BESS and PV systems application for optimal microgrid operation with frequency security constraints

Bagheri-Sanjareh, Mehrdad; Popov, Marjan

DOI
10.1016/j.segan.2025.102103

Publication date
2026

Document Version
Final published version

Published in
Sustainable Energy, Grids and Networks

Sustainable Energy, Grids and Networks 45 (2026) 102103

Contents lists available at ScienceDirect

Sustainable Energy, Grids and Networks

journal homepage: www.elsevier.com/locate/segan

BESS and PV systems application for optimal microgrid operation with frequency security constraints

Mehrdad Bagheri-Sanjareh *, Marjan Popov

Delft University of Technology, Faculty of EEMCS, Mekelweg 4, Delft 2628CD, the Netherlands

ARTICLE INFO

Keywords:
Microgrid
Battery energy storage system (BESSs)
Lithium-ion battery
Photovoltaic systems
Frequency control
Optimal operation
Energy management
Optimization

ABSTRACT

Battery energy storage systems (BESSs) have been used in AC Microgrids (AMGs) for frequency control (FC) and energy management (EM). AMGs with low inertia might suffer large frequency deviations with high rates without the required reserve power for FC. This paper proposes a linear model for the optimal operation of grid-connected AMGs considering frequency security constraints. BESS and photovoltaic systems both participate in primary FC (PFC) and EM. PVSs can decrease their generation in power surplus conditions. They can release the energy of their DC-link capacitors in power shortage conditions. Through coordinated use of BESS and PVSs, the required BESS power for PFC decreases considerably, which allows the BESS to participate in EM more effectively and hence reduces the AMG operational cost. Frequency simulation studies show that PVSs can considerably assist BESS for PFC. Moreover, the optimization results show that without PVSs' support, load shedding is unavoidable which increases the AMG operation cost significantly. In this regard, deterministic and stochastic optimization show that PVSs' participation in PFC results in 24 % and 24.2 % reduction in the AMG operation cost compared to those when BESS is only used for PFC. Therefore, the PVSs' assist in PFC, even though short, has large impact on the optimal operation of the AMG.

1. Introduction

1.1. Microgrid, its components and modes of operation

Renewable energy sources such as photovoltaic systems (PVSs) play a vital role in clean energy generation. Their proliferation in distribution networks has facilitated the formation of Microgrids (MGs). In addition to PVSs, other types of distributed generators (DGs), such as diesel generators and energy storage systems (ESSs) have been widely used in MGs [1]. In AC grids, MGs operate either in grid-connected mode or islanded mode [2].

Due to the increased penetration of renewable resources, the overall inertia of grids is decreasing, leading to faster frequency variations [3,4]. As MGs have relatively less inertia, their frequency variations are more severe than bulk power systems, showing the necessity of reliable FC schemes for AC MGs (AMGs) [5], which ensure the power balance between the supply and demand [6]. The power exchange with the upstream grid prevents any power shortage or surplus in the AMG; hence, the AMG frequency remains stable. The optimal AMG operation is ensured through this power exchange and the generation control of AMG energy resources like distributed generators (DGs) and the ESSs [7].

1.2. BESS's role in AMG frequency regulation and energy management

The ESSs can absorb and release energy when energy prices are low and high, respectively, to decrease the AMG operational cost. However, an unintentional islanding stops the power exchange with the upstream network, and consequently upsets the AMG demand-supply balance [8]. Fast frequency response is imperative to maintain the frequency stability of the islanded low-inertia AMG [9]. The generation of distributed generators (DGs) cannot be instantly changed to restore the balance. Conversely, energy storage systems (ESSs) can do this, making them suitable for primary FC (PFC). For secondary FC (SFC), dispatchable DGs are used, which restore the frequency to the nominal value [10].

Battery ESSs (BESSs) are commonly used for grid applications [11]. They are used for both PFC [12] and energy management (EM) [13,14] in isolated grids such as AMGs. One BESS is capable of both tasks. BESS can emulate the response of a synchronous generator by controllers like the droop characteristics using which BESS power can be decreased or increased in case a frequency rise or drop occurs [15]. On the other

* Corresponding author.
E-mail addresses: M.Bagheri-sanjareh@tudelft.nl (M. Bagheri-Sanjareh), M.Popov@tudelft.nl (M. Popov).

https://doi.org/10.1016/j.segan.2025.102103
Received 14 October 2025; Received in revised form 26 November 2025; Accepted 18 December 2025
Available online 19 December 2025

Nomenclature

Abbreviations and symbols

AMG	AC microgrid
BESS	Battery ESS
D	Duty cycle
DEG	Diesel generator
DG	Distributed generator
DIM	Dimension
DLC	DC-link capacitor
DLCV	DLC voltage
EM	Energy management
ESS	Energy storage system
f_{AMG}	AMG frequency
f_0	AMG nominal frequency
FC	Frequency control
FCUC	Frequency-constrained unit commitment
FD	Frequency deviation
FDB	Frequency dead-band
f_{max}	Maximum frequency rise
FR	Frequency regulation
H_{AMG}	Overall AMG inertia
HPF	High-pass filter
MILP	Mixed-integer linear programming
MP	Maximum power
MPP	MP point
MPPT	MPP tracking
P_{em}	Active power reference for EM
PFC	Primary FC
P_D	Power demand
P_{fr}	Active power reference for frequency regulation
P_G	Power generation
P^r_{PVS}	PVS rated power
P_{PVS}	Actual power generation of PVS
P_{ref}	BESS active power reference
PVS	Photovoltaic system
RoCoF	Rate of change of frequency
SFC	Secondary FC
SOFC	Solid-oxide fuel cell

Sets and indices

g	Set of non-renewable DGs
g1	Set of renewable DGs
i	Index used to linearize battery degradation cost
m,n,k	Represent dimensions of 3-DIM table that represents required BESS power for PFC
t/T	Index/set of time periods

Parameters

a_g,b_g,c_g	Cost coefficients of non-renewable DGs
CB^P,CB^E	Power and energy rating cost of battery
d_g,e_g,f_g	Penalty emission cost coefficients of non-renewable DGs
$DOD_i^{\min}/DOD_i^{\max}$	Minimum/maximum values of DOD in each segment
EB^r	BESS rated capacity
F_G	Operation cost function of dispatchable DGs
M_g,M_{g1}	Maintenance cost coefficients of DGs
N_{cycle}	Battery number of life cycles
N_{sg}	number of synchronous generators
$PDG_g^{\min},PDG_g^{\max}$	Minimum and maximum power limits
PB^r,EB^r	Power and capacity rating of battery
π_b/π_s	Price of buying/selling energy
UCg,DCg	Start up and shut down cost of DGs
$V_i^{\min}/V_i^{\max}$	Minimum/maximum values of each segment of LCCBt
η_{BESS}	BESS efficiency
ρ_S	Probability of scenario

Variables

CDBAT	Battery degradation cost
CLS	Load shedding cost
CUG	Power exchange cost of with the utility grid
DOD_t	Depth of discharge
EB_t^{df}/EB_t^{cf}	Required SOC for discharge/charge for PFC
IC_t	Avoids simultaneity of discharge and charge
IU_t	Avoids simultaneity of buying and selling grid power
$LCCB_t$	Battery life cycle cost
OCDGS	Operation cost of the DGs
PB_t	Overall BESS power
PB_t^d/PB_t^c	BESS power discharge/charge
PB_t^{dcmf}	Required BESS power for PFC
$PB_t^{\max}$	Maximum limit for BESS power
PD_t	Power demand
$PDG_{g,t}$	DGs generated power
PLS_t	Shed load
PUG_t	Overall exchanged power with utility grid
PUG_t^b,PUG_t^s	Bought/sold grid power
$PUG_t^{\max}$	Maximum limit for utility grid power
$SUC_{g,t}$	Start-up cost
$SDC_{g,t}$	Shut-down cost
$S_{g,t}$	On/off state
SOC_t	Battery state of charge
TOCA	AMG operation cost
WW	Used to include unfinished discharge cycle
$W_{n,k,t}$	Used for interpolation
$Y_{i,t}$	Auxiliary variable used for linearizing
YY_t/ZZ_t	Used to detect start/end of each discharge cycle
$Z1_t$	Auxiliary variable used for linearizing

hand, EM relies on longer-term operation optimization rather than fast real-time response. This includes peak shaving, load shifting and economic dispatch which can be realized by day-ahead or intra-day optimization [16].

As the frequency regulation has priority over the energy management, the frequency constraints should be met in grid-connected operation optimization. This ensures the AMG frequency stability in case of an unplanned islanding. In this regard, the authors of [17] and [18] have proposed frequency stability-constrained economic dispatch of DGs and BESSs to optimize the MG operation after forced islanding. According to their proposed scheme, a significant portion of the BESS power must be reserved for FC. This makes a part of the BESS power discharge/charge capability unavailable, which adversely affects BESS's role in the EM.

1.3. PVSs' role in AMG frequency regulation

Use of PVSs for PFC allows more participation of the BESS in the EM. The authors of [19,20] have proposed curtailing the PVS's power to provide PFC in power shortage situations by releasing the curtailed power. However, the drawbacks of this approach is not generating the maximum power (MP) and estimating the MP point (MPP) under different climate conditions. The second approach is the use of a dump load [20,21]. The third approach is to lower the PVSs generation below the MPP [22,23]. The second and third approaches are only applicable

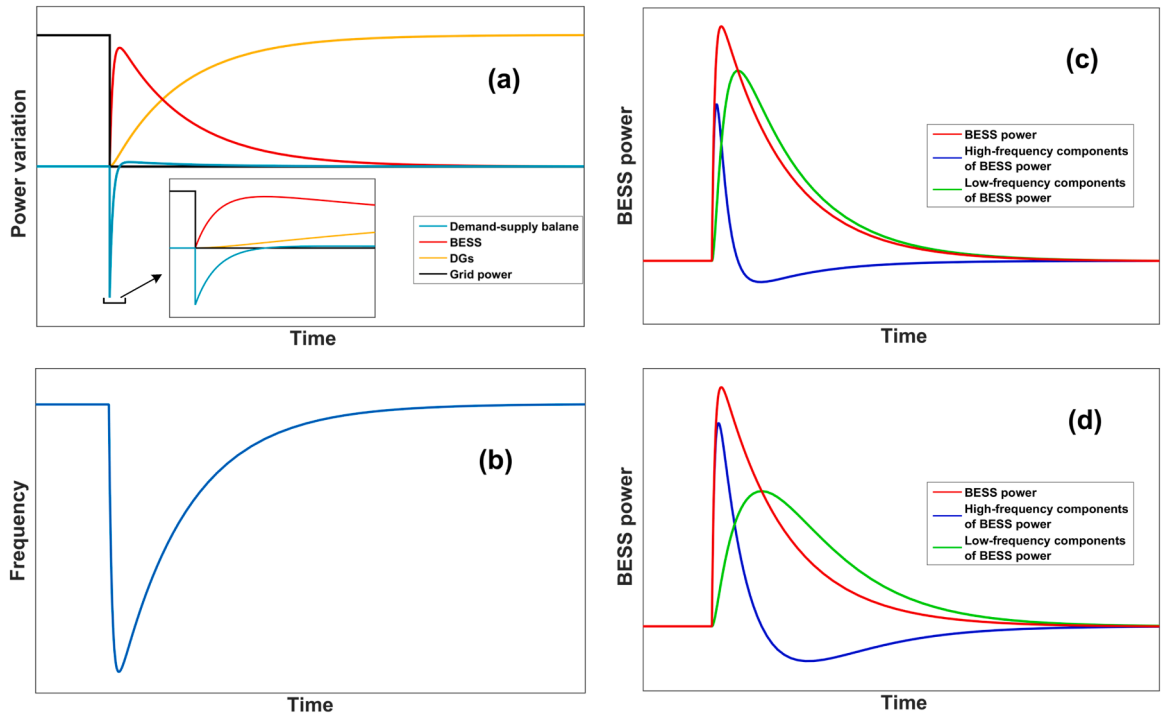

Fig. 1. AMG frequency response, (a) power variations of resources, (b) AMG frequency, (c) Decomposed BESS power (high- and low-pass filters time constants = 0.3 s), (d) Decomposed BESS power (filters time constants = 1 s).

when the frequency rises due to power surplus [20]. The fourth approach releases the stored energy of the DC-link capacitors (DLCs) of PVSs to manage the power shortage [24]. However, the DC-link capacitor has a limited capacity that leads to the fifth approach, in which a supercapacitor is used instead in the DC-link [25]. The drawback of the fourth and the fifth approaches is that they inhibit the PVSs from operating at MPP by preventing the DC-link voltage from being constant for MPP tracking (MPPT). The coordination of BESS and PVSs have been considered in [26] to provide PFC. However, the authors have proposed curtailment of PVSs for providing frequency support which is inefficient similar to the first approach.

To overcome the mentioned drawbacks, a new FC scheme is proposed for PVSs. During power shortage conditions when the frequency drops, the DLCs are used to provide PFC shortly alongside the BESS. A frequency dead-band (FDB) and a high-pass filter (HPF) make the PVSs to respond only to extreme frequency disturbances. In power surplus conditions, the PVSs are controlled to decrease their power output proportionally to the frequency rise. The FDB prevents the PVSs from responding to the low-frequency rises. The use of FDBs and HPFs hardly makes the PVSs deviate from MPP for frequency regulation, which makes it more efficient compared to the first, third and fourth approaches. In contrast to the fifth approach, the supercapacitors is not used. Despite the limited energy injection by the DLC, it is sufficient to enable PVSs participation in PFC. The proposed approach in this paper for PVSs frequency regulation decreases the required BESS power reserve for PFC, which allows more participation of the BESS in EM.

1.4. MG optimal operation with frequency security constraints

Some of recent research works on the optimal operation have considered frequency stability constraints. The authors of [27] have addressed the frequency-constrained unit commitment (FCUC) problem. In [28], the FCUC problem is solved with the help of neural networks that determine the virtual inertia parameters and droop coefficients, while the authors of [29] have instead considered spatial differences in frequency deviations (FDs). Reference [30] deals with the FCUC problem with the aim of enhancing frequency stability for an isolated network. The works conducted by [17,18] have tried to solve the problem of optimal AMG operation with frequency security constraints. These two papers have not modeled the battery degradation cost. The authors of [31] have used optimal power flow to minimize the difference between the costs of the scheduled operation and the operation that considers frequency security after islanding. The drawback of their work is that their formulated problem contains differential algebraic equations which are nonlinear. In [32], optimal scheduling of a power system, which contains hydropower, wind and PVSs, is considered with security frequency constraints. The problem is formulated with nonlinear constraints. A common drawback of the research works in [28–30,32] is that the role of ESSs is not considered. References [17,18, 28–32] cannot obtain the global optimal solution due to the nonlinearity arising from the multiplication of network inertia and FD, as they are continuous variables. This issue is not considered by [17]. Furthermore, the authors in [18] have used a penalty function to ensure frequency security, which either does not properly enforce the frequency security requirement or prevents the solution from being optimal. The authors have also considered equal time constants for the BESS and Diesel generators (DEGs) models which is not correct. It is of note that BESS mainly consists of static elements and thus its time constants are much smaller compared to the DEGs. Because of this, the accuracy of the results in [18] remains a question, too. Last but not least, none of these works have used the PVS's potential in PFC.

1.5. Summary

This article will solve the above mentioned issues. A comprehensive frequency simulation study is conducted to obtain the required BESS reserve power for PFC with PVSs participation under different operation conditions. Then, the obtained data is used for the frequency constraints of the optimal AMG operation. Therefore, the frequency security is always ensured while minimizing the AMG operation cost. It is worth noting that the proposed model is fully linear. Besides, it is much simpler and faster as frequency simulation studies are done just once, and before

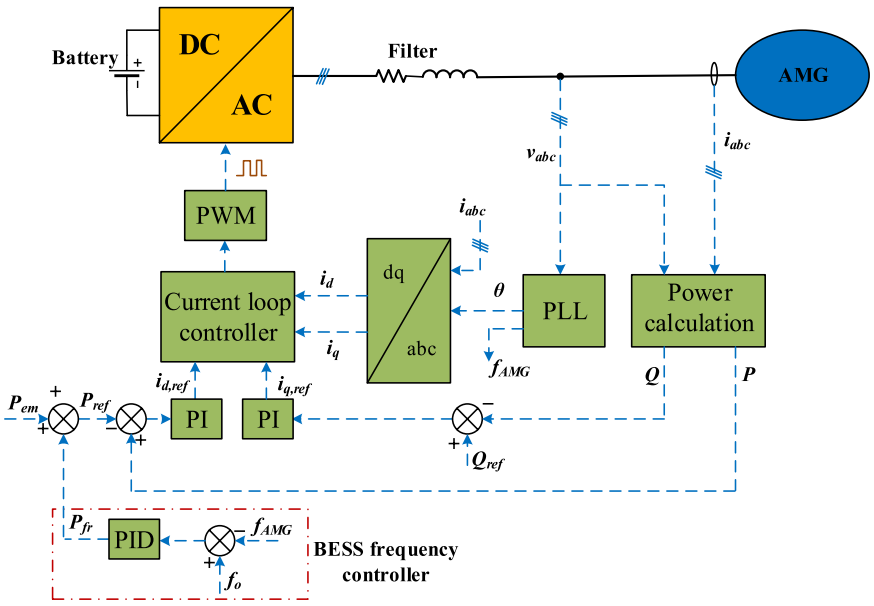

Fig. 2. BESS configuration and its control.

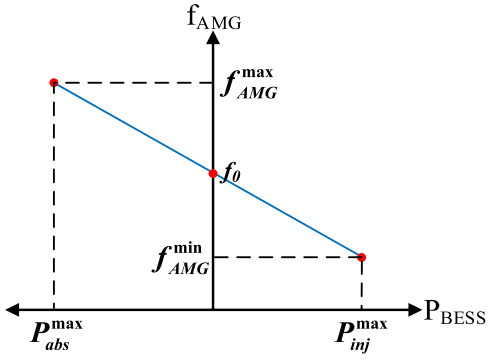

Fig. 3. BESS PFC characteristics.

the optimization.

The shortage of previous works and the contribution of this paper are summarized below:

- To our knowledge, no research work has ever used the coordinated application of BESS and PVSs and the usage of FDBs and HPFs for reducing the AMG operation cost while maintaining its frequency stability.
- The DC-link supercapacitor is not required for the PVSs to perform PFC.
- The proposed PVS control, which uses FDBs and HPFs, ensures operation at the MPP except shortly for PFC when power surplus occurs.
- Unlike previous papers with the nonlinearity problem, the model of this paper is completely linear.
- BESS degradation cost is modelled in the AMG cost optimization problem as opposed to the previous papers which either have missed it out or have not used ESSs entirely.
- Frequency security requirements are modelled directly as constraints which guarantees both the solution optimality and the frequency security.

The paper is organized as follows: the AMG frequency dynamics and control schemes of BESS and PVSs are presented in Section 2. Section 3 discusses and formulates the AMG operation costs and the frequency security constraints. Section 4 presents the studied AMG network and frequency simulation results. The results of these studies are summarized and used for solving the optimal AMG operation problem in Section 5 with the applied frequency constraints defined in Section 4. Section 6 concludes the paper.

2. Proposed FC scheme using BESS, PVs, and DGs

The AMG frequency is governed by Eq. (1) [33]:

$$df_{AMG}/dt = \left(f_0/2H_{AMG}\right) \times (P_G - P_D) \quad (1)$$

where f_{AMG} is the AMG frequency and f_0 is its rated value. H_{AMG} represents the overall AMG inertia whereas P_D, and P_G are respectively the total power demand and generation.

Fig. 1 depicts the AMG frequency dynamics after unintentional islanding while receiving power from the utility grid. The quick power discharge of BESS intercepts the frequency drop and with the help of DGs, the frequency is restored to its rated value. A large part of the BESS power decreases momentarily. Fig. 1(c) and (d) show the BESS power decomposed into fast and slow components. It is evident that the fast component mostly causes the peak BESS power. If another device (which is the PVSs in this work) provides the fast component, the BESS peak power would decrease which allows more participation of the BESS in EM.

Secondary FC (SFC) using dispatchable DGs is explained in [34]. The role of BESS and PVSs in PFC is discussed in the following.

2.1. BESS control scheme for PFC

Fig. 2 shows the BESS configuration. The reference active power (P_{ref}) consists of the reference active powers of EM and PFC, which are denoted by P_{em} and P_{fr}, respectively. The BESS injects/absorbs power to/from the AMG to control the frequency after a power shortage or surplus. The derivative of the BESS PID controller provides the virtual inertia, which decreases the rate of change of frequency (RoCoF). The integral component is set to zero since dispatchable DGs, and not BESS, mainly restore the frequency. The performance of the proportional component of the PID controller is shown in Fig. 3. The derivative and the proportional parts behave similarly except that the former only responds to the RoCoF.

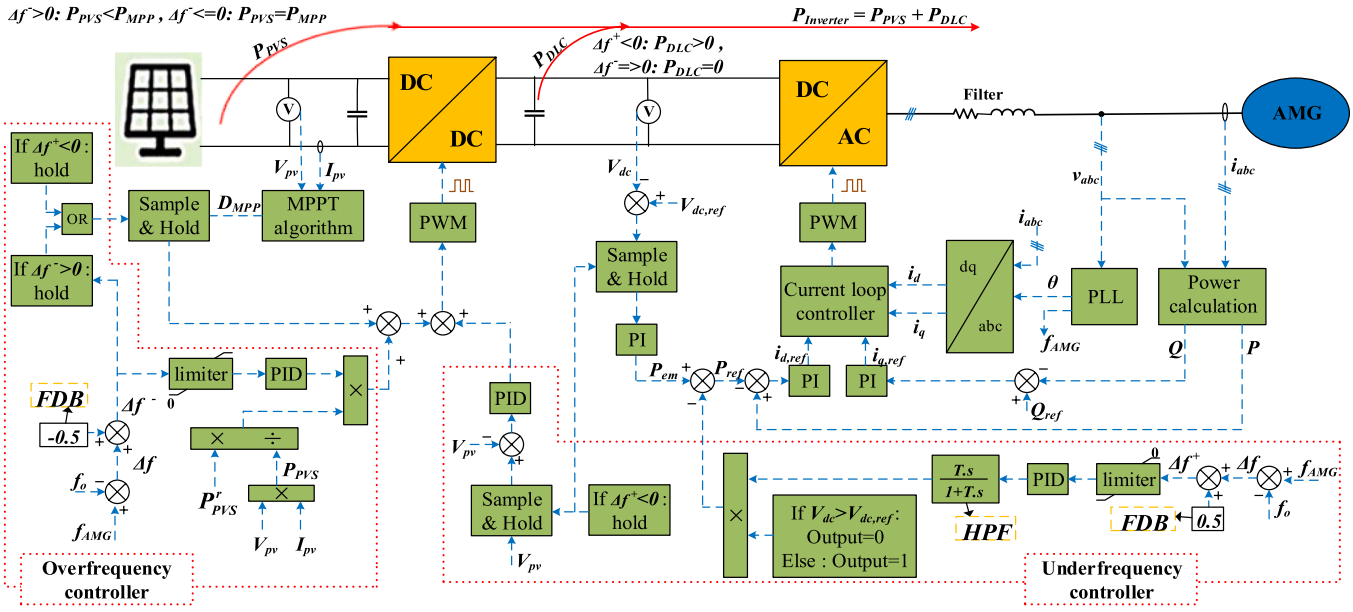

Fig. 4. PVS configuration and its control system.

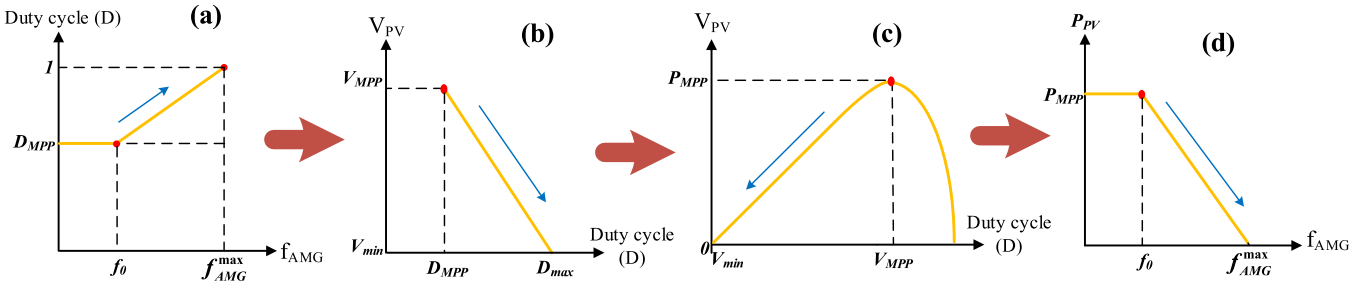

Fig. 5. FC strategy of the PVS for power surplus conditions.

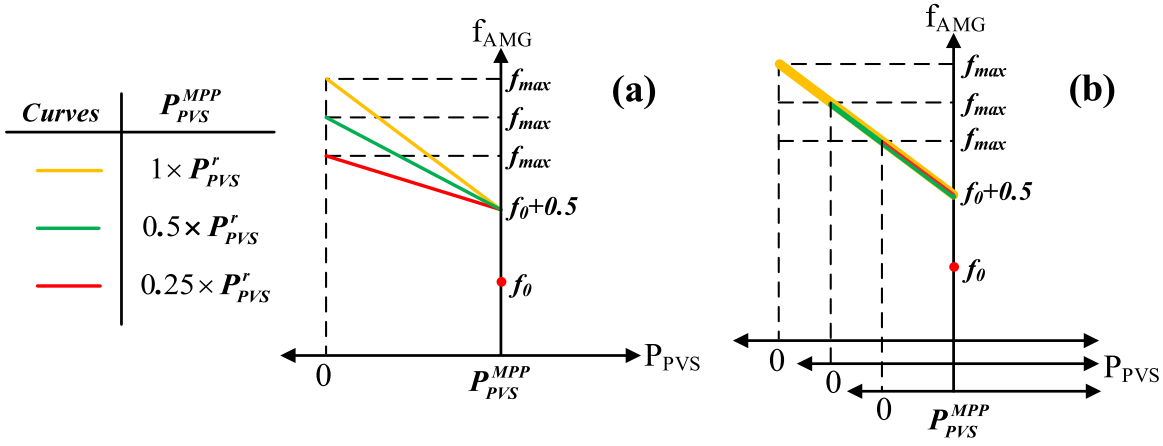

Fig. 6. FC (proportional component) characteristic of the PVS, (a) Not normalized, (b) Normalized.

2.2. PVSs control scheme for PFC

The PVS configuration is shown in Fig. 4. The frequency controller, which is shown on the left side, controls the power surplus, whereas the other, the power shortage.

The PVSs control strategy for power surplus conditions is shown in Fig. 5. Normally, the duty cycle (D) of the PVS converter extracts MPP from PV arrays. However, in case of power surplus conditions, the D can be increased as shown in Fig. (5-a). Figs. (5-b) and (5-c) show that this leads to decreasing the PV voltage and power from the MPP. The decrease in the PVS power is proportional to the FD as depicted in Fig. (5-d). The left side of power-voltage curve as proposed in [23].

According to Fig. 4, the MPPT algorithm ensures that the MPP is extracted from the PV array. In case the frequency increases above the upper bound of FDB (50.05 Hz), D is held constant to be modified for PFC. The MPPT algorithm control loop is temporarily disabled to avoid

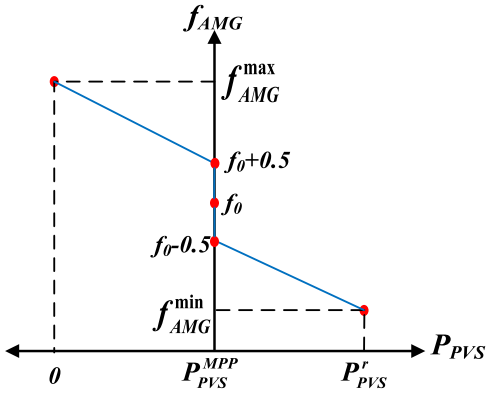

Fig. 7. FC (proportional component) characteristics of the PVS for power shortage conditions.

conflict between the PFC and the MPPT algorithm control loops. It is assumed that during the very short period of the PFC, the MPP is constant. The frequency restoration activates the MPPT algorithm loop again and deactivates the PFC loop.

The PFC signal is normalized by multiplying and dividing the control signal by the PVS rated power (P_{PVS}^{r}) and its actual power generation (P_{PVS}), respectively. Fig. 6 compares the performance of the proportional component of the PID when the PFC signal is normalized or not. Fig. (6-a) shows that without normalization, the MPP is not fully utilized for PFC unless the frequency reaches its maximum value (f_{max}). On the other hand, Fig. (6-b) shows that the normalization allows full use of MPP as the power reduction slope is constant regardless the MPP variations.

The PFC strategy during power shortage conditions is as follows. In normal conditions, the inverter ensures that MPP is delivered to the AMG by maintaining the DLC voltage (DLCV) at the reference value (V_{dc_ref}). When a power shortage occurs, the PID controller makes the DLC release its energy to the AMG if the frequency drops below the lower bound of the FDB (49.95 Hz). The HPF is used to decrease the DLC energy discharge by responding only to high-frequency components (HFCs) of FDs. The HPF time constant is denoted by T. During the PFC period, the input of the DLCV controller of the inverter is blocked to avoid the conflict with the PFC loop. Moreover, another PID controller is used to control the D to keep the PV array voltage at the value of MPP while the DLCV varies due to the release of DLC energy.

Without the FDB, the PVS hardly operates at MPP due to the continual occurrence of small frequency disturbances. Therefore, the FDB usage helps the PVS to operate at MPP except for a few short PFC periods. The integrators of PID controllers are not used since PVS participates in PFC and not SFC. Fig. 7 shows the performance of the proportional components of both PVS frequency controllers. Unlike the proportional components, the derivatives of the PID controller only respond to the RoCoF.

Considering that power shortage and surplus generation conditions do not occur simultaneously, the two FC loops are independent. However, they depend on the MPP as a higher MPP allows more downward power regulation while limiting upward regulation as the inverters are closer to their rated power.

3. Proposed frequency security-constrained EM (FCEM) scheme

The EM aims to minimize AMG operation cost (*TOCA*) in grid-connected mode as presented in Eq. 2. It consists of the operation cost of the DGs (*OCDGS*), the cost of power exchange with the utility grid (*CUG*), the battery degradation cost (*CDBAT*), and the load shedding cost (*CLS*).

$$Min\{TOCA = OCDGS + CUG + CDBAT + CLS\} \tag{2}$$

3.1. DGs cost

The operation cost of the dispatchable DGs is modelled using Eqs. (3) and (4):

$$OCDGS = \sum_{t\in\Omega_T}\sum_{g\in\Omega_{DG}} F_G\left(PDG_{g,t}\right) + \sum_{t\in\Omega_T}\sum_{g\in\Omega_{DG}}\left(SUC_{g,t} + SDC_{g,t}\right) + \sum_{t\in\Omega_T}\sum_{g1\in\Omega_{RG}}\left(M_{g1}\times PRG_{g1,t}\right) \tag{3}$$

$$\begin{cases} F_g\left(PDG_{g,t}\right) = \left(a_g PDG_{g,t}^2\right) + \left(b_g PDG_{g,t}\right) + c_g + \left(\left(d_g + e_g + f_g + M_g\right)PDG_{g,t}\right) \\ \forall g \in \Omega_{DG} \end{cases} \tag{4}$$

where F_G and $PDG_{g,t}$ are the cost function and the generated power of the g^{th} non-renewable DG, respectively and a_g, b_g and c_g are its cost coefficients. Coefficients d_g, e_g and f_g represent the penalty emission cost of CO_2, SO_2, and NOx. M_g and M_{g1} represent the maintenance cost coefficient of non-renewable and renewable DGs, respectively. $SUC_{g,t}$ and $SDC_{g,t}$are the start-up costs and shut-down costs of DG units. The piecewise linearization approach in [35] is used to linearize the DGs cost function.

Eq. (5) models the generation limits of dispatchable units:

$$S_{g,t}PDG_g^{\min} \le PDG_{g,t} \le S_{g,t}PDG_g^{\max} \tag{5}$$

where $PDG_g^{\min}$ and $PDG_g^{\max}$ are the maximum and minimum power limits of the g^{th} DG, whereas binary variable $S_{g,t}$ represents the on/off state.

The start-up and shut-down costs are modelled by Eqs. (6) and (7):

$$UC_g\left(S_{g,t} - S_{g,(t-1)}\right) \le SUC_{g,t} \quad , \quad 0 \le SUC_{g,t} \tag{6}$$

$$DC_g\left(S_{g,(t-1)} - S_{g,t}\right) \le SDC_{g,t} \quad , \quad 0 \le SDC_{g,t} \tag{7}$$

where UC_g and DC_g are the constant costs of starting up and shutting down the i^{th} DG unit.

3.2. Grid cost

The operation cost of the power exchange with the utility grid is modelled using Eq. (8):

$$CUG = \sum_{t\in\Omega_T}\left(\pi_b PUG_t^b - \pi_s PUG_t^s\right) \tag{8}$$

where π_b/π_s are the prices of buying/selling energy from/to the utility grid. Variables

PUG_t^b/PUG_t^s represent the power bought/sold from/to the utility grid. The overall exchanged power with the utility grid (PUG_t) is presented in Eq. (9):

$$PUG_t = PUG_t^b - PUG_t^s \tag{9}$$

Binary variable IU_t and Eqs. (10) and (11) prevent the simultaneity of buying and selling:

$$PUG_t^b \le PUG_t^{\max} IU_t \tag{10}$$

$$PUG_t^s \le PUG_t^{\max}(1 - IU_t) \tag{11}$$

where $PUG_t^{\max}$ is the maximum limit for utility grid power exchange.

3.3. BESS operation limits

The maximum limits for BESS power discharge/charge (PB_t^d/PB_t^c) are presented in Eq. (12).

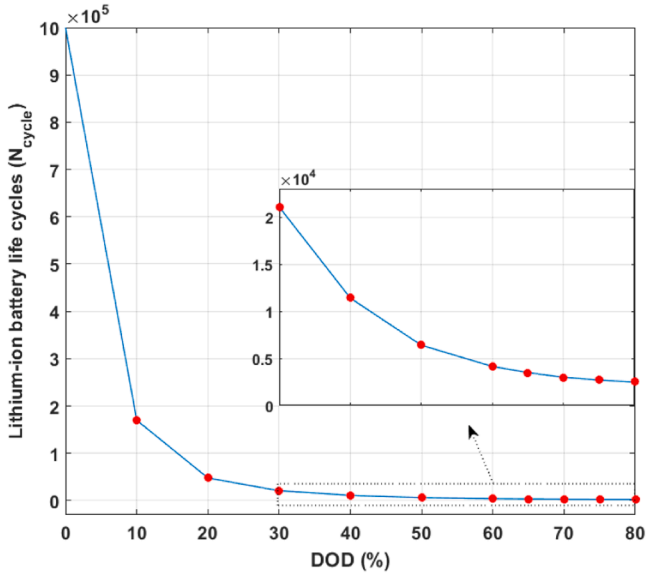

Fig. 8. Lithium-ion battery life cycle vs. DOD.

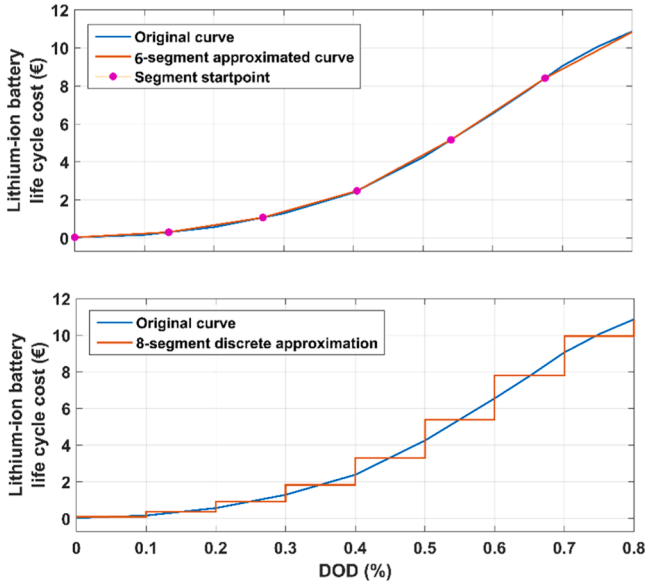

Fig. 9. Approximation of the LCCB curve.

$$0 \le PB_t^d / PB_t^c \le PB_t^{\max} \tag{12}$$

where $PB_t^{\max}$ is the maximum allowable limit for BESS power in both charge and discharge modes.

Eq. (13) models the overall BESS power (PB_t):

$$PB_t = PB_t^d - PB_t^c \tag{13}$$

Binary variable IC_t in Eqs. (14) and (15) prevent the simultaneity of charging and discharging:

$$PB_t^c \le PB^{\max} IC_t \tag{14}$$

$$PB_t^d \le PB^{\max}(1 - IC_t) \tag{15}$$

Battery state of charge (SOC_t) is calculated by Eq. (16):

$$SOC_t = SOC_{(t-1)} + \left(PB_t^c / (EB^r \eta_{BESS})\right) - \left(\left(PB_t^d \eta_{BESS}\right) / (EB^r)\right) \tag{16}$$

where EB^r is the rated capacity of the BESS whereas η_{BESS} is the BESS efficiency. Eq. (17) models the SOC_t limits. The minimum and maximum limits in this equation are taken from [36].

$$0.2 \le SOC_t \le 1 \tag{17}$$

3.4. Demand-supply balance constraint

Eq. (18) presents the demand-supply balance:

$$\sum_{g \in \Omega_{DG}} PDG_{g,t} + \sum_{g1 \in \Omega_{RG}} PRG_{g1,t} + PUG_t - PD_t + PLS_t = 0 \qquad \forall t \in \Omega_T \tag{18}$$

where, PD_t is the power demand and PLS_t denotes the shed load.

3.5. Battery life cycle cost

A fixed cost based on €/kWh is commonly used to represent *CDBAT*. However, this paper follows a more precise approach like some other research. In this regard, *CDBAT* depends on various factors such as depth of discharge (*DOD*) which is considered in [37] as the main degradation factor. Fig. 8 shows the life cycle of a typical Lithium-ion battery concerning *DOD* variation using data available in [38].

The life cycle cost per *DOD* (*LCCB*) can be calculated using Eq. (19) [37]:

$$LCCB = \left(CB^P PB^r + CB^E EB^r\right) / \left(N_{cycle}\right) \tag{19}$$

where CB^P and CB^E are the power and energy rating cost of the battery for a lithium-ion battery are 278.4€/kW and 313.2€/kWh, respectively, according to [38]. PB^r and EB^r are power and capacity rating of the BESS. N_{cycle} is the number of life cycles. Therefore, a 30 kW/60kWh Lithium-ion battery costs € 27144. Fig. 9 shows the value of *LCCB* for different values of N_{cycle}. The original curve is directly derived by dividing €27144 by the data of Fig. 8. To calculate *LCCB* for each segment, two approaches can be used as shown in Figs. (9-a) and (9-b). The first approach (a) uses 1st-order functions with different slopes and start points to approximate different segments, while the second approach allocates the average value of each segment. The first approach is used as it is more accurate.

Binary variable $Y_{i,t}$ in Eqs. (20) and (21) help to choose only one segment in Fig. 9 using the value of *DOD* at each time step (DOD_t).

$$\sum_{i \in \Omega_{6s}} DOD_i^{\min} Y_{i,t} \le DOD_t \le \sum_{i \in \Omega_{6s}} DOD_i^{\max} Y_{i,t} \tag{20}$$

$$\sum_{i \in \Omega_{6s}} Y_{i,t} = 1 \tag{21}$$

where $\sum_{i \in \Omega_{6s}} DOD_i^{\max} Y_{i,t}$ and $DOD_i^{\max}$ are the minimum and maximum values of DOD_t in the i^{th} segment. Then, the value of $LCCB_t$ is calculated using Eq. (22):

$$\begin{cases} LCCB_t = \sum_{i \in \Omega_{6s}} \left(\left(\left(V_i^{\max} - V_i^{\min} \right) / \left(DOD_i^{\max} - DOD_i^{\min} \right) \right) \times \left(DOD_t - DOD_t^{\min} \right) + V_i^{\min} \right) \times Y_{i,t} \right) \\ \qquad \forall t \in \Omega_T \end{cases} \tag{22}$$

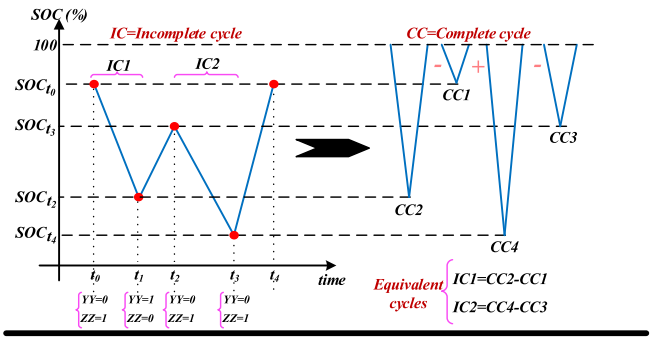

Fig. 10. Rainflow counting algorithm for battery cost calculation.

where $V_i^{\max}$ and $V_i^{\min}$ are the maximum and minimum values of $LCCB_t$ in the i^{th} segment. The multiplication of DOD and $Y_{i,t}$ makes Eq. (22) nonlinear. Eqs. (23–25) eliminate the nonlinearity by substituting the multiplication term with the auxiliary variable$Z1_t$, considering the maximum and minimum values of DOD_t are 80 % and 0 %, respectively.

$$0 \le Z1_t \le 80 Y_{i,t} \tag{23}$$

$$Z1_t \le DOD_t \tag{24}$$

$$Z1_t \le DOD_t - 80\left(1 - Y_{i,t}\right) \tag{25}$$

The values of N_{cycle} in Fig. 8 are for full SOC discharge cycles. However, batteries experience incomplete discharge cycles too. The rainflow algorithm, discussed in [39] and shown in Fig. 10, can convert the incomplete cycles to the complete cycles, which is mathematically modelled by Eqs. (26–28).

$$IC_{(t-1)} - IC_t + YY_t - ZZ_t = 0 \tag{26}$$

$$YY_t + ZZ_t \le 1 \tag{27}$$

$$\sum_{t \in \Omega_T} YY_t - ZZ_t + WW = 0 \tag{28}$$

where binary variables YY_t and ZZ_t detect the start of discharge and charge cycles, respectively, by becoming 1 as exemplified in Fig. 10. Finally, Eq. (29) calculates $CDBAT$:

$$CDBAT = \left(\sum_{t \in \Omega_T} LCCB_t \times \left(YY_t - ZZ_t\right)\right) + \left(LCCB_{t=t_e} WW\right) \tag{29}$$

In case, a discharge cycle is not finished by the end of the last interval, the binary variable WW includes the cost of the last discharge cycle $LCCB_{t=t_e}$, in which t_e denotes the last interval.

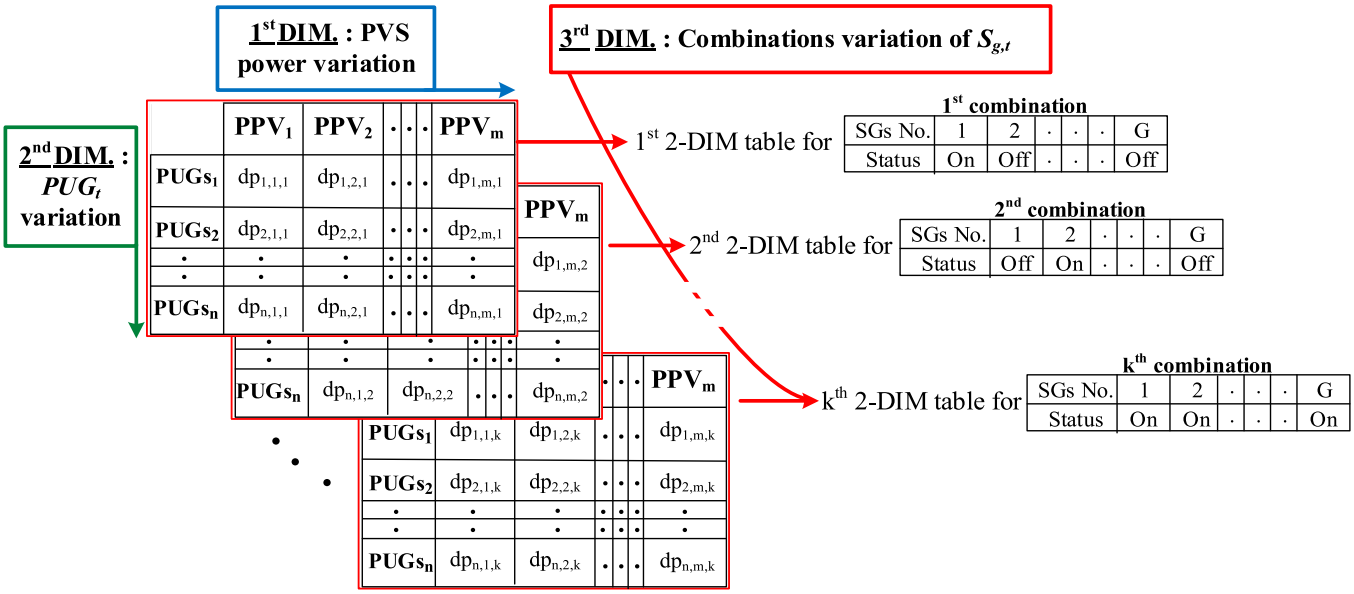

Fig. 11. 3-DIM table representing the PB_t^{dcmf}.

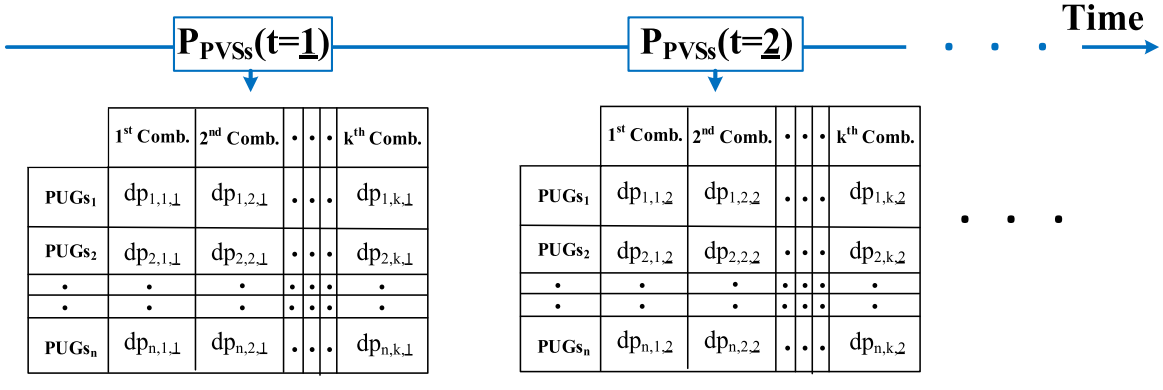

Fig. 12. 2-DIM tables representing the PB_t^{dcmf} at each interval.

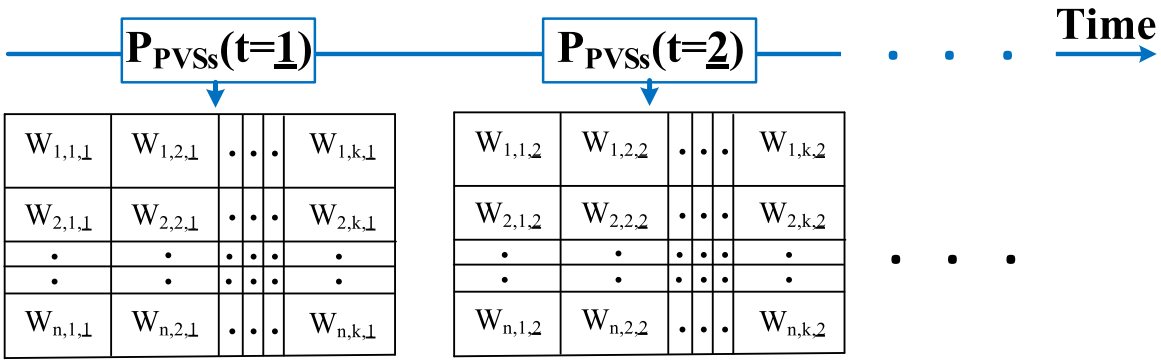

Fig. 13. Structure of binary variable $W_{n,k,t}$ at each interval.

3.6. Frequency security constraint

The frequency constraints in the case of unintentional islanding are as follows. The absolute FD and the RoCoF should be within the permissible limit, which are 1 p.u (0.5 Hz for 50 Hz system) and less than 2.5 Hz/s, respectively [23,40]. According to Eq. (1), the overall AMG inertia and the disturbance determine the FD and the RoCoF. The AMG needs enough inertia to keep the RoCoF within limits as PUG_t varies. Also, the response of BESS and PVSs and the combination of the variations of $S_{g,t}$ affect the overall AMG inertia. The PFC controllers of the PVSs are assumed to be tuned once and they are invariable afterwards. However, the BESS which can be instantly controlled by the AMG central management. Considering these explanations, Eqs. (30) and (31) present the frequency constraints for the BESS maximum power for EM.

$$PB_t^d \le PB^{\max} - PB_t^{dcmf} \tag{30}$$

$$PB_t^c \le PB^{\max} + PB_t^{dcmf} \tag{31}$$

where PB_t^{dcmf} is the required BESS power for PFC, which is determined using the table with 3 dimensions (DIMs) as shown in Fig. 11. The first dimension (1st-DIM) of the table represents PVSs' power variation, the second dimension (2nd-DIM) represents the variations of PUG_t and the third dimension (3rd-DIM) accounts for the combination of variations of $S_{g,t}$. Sets *m,n* and *k* are used to represent each dimension, respectively.

Since PVSs power is not a variable, the 1st-DIM can be removed from the 3-DIM table, and instead, a 2-DIM table can be obtained for each time interval, as shown in Fig. 12. The 2-DIM tables vary as PVSs power varies over time. A single value in each 2-DIM table can be found for PB_t^{dcmf} by interpolating between the segments of 2nd-DIM, considering that interpolation is not required for the 3rd-DIM as $S_{g,t}$ is a binary variable.

Binary variable $W_{n,k,t}$ selects one column and two consecutive rows of 2-DIM tables at each interval, which are required for interpolation. Having *n* rows leads to (*n-1*) range that can be chosen for interpolation. The structure of $W_{n,k,t}$ is shown in Fig. 13.

Eq. (32) selects one column of the 2-DIM table which depends on the values of $S_{g,t}$:

$$\prod_{g\in\Omega_{Nsg}} \left(U_{k,g2} + H_{k,g2} S_{g2,t} \le W_{n,k,t}\right) \qquad \forall t \in \Omega_T, \forall k \in \quad \Omega_{Comb}, \forall t \in \Omega_{PUGseg} \tag{32}$$

where $U_{k,g2}$ and $H_{k,g2}$ are matrices that are used to represent all possible combinations of $S_{g,t}$. The elements of these matrices are simultaneously either (0,1) or (1, −1). When one combination is realized, the left side of Eq. (32) becomes equal to 1. This makes the single element of $W_{n,k,t}$, which corresponds to that combination, to becomes 1 too.

To illustrate how Eq. (32) works, Eq. (33) presents this constraint for two synchronous generators (SGs). For N_{sg} number of SGs, we would have $\left(2^{N_{sg}} - 1\right)$ number of combinations of $S_{g,t}$ which excludes the one in which all SGs are simultaneously off. This is done to avoid having zero inertia. In this case, the number of combination is $\left((2^2 - 1) = 3\right)$.

$$U_{3,2} = \begin{bmatrix} 0 & 1 \\ 1 & 0 \\ 0 & 0 \end{bmatrix}, H_{3,2} = \begin{bmatrix} 1 & -1 \\ -1 & 0 \\ 0 & 0 \end{bmatrix} \rightarrow \begin{cases} S_{(g=1),t}\left(1 - S_{(g=2),t}\right) \le W_{n,1,t} \\ \left(1 - S_{(g=1),t}\right) S_{(g=2),t} \le W_{n,2,t} \\ S_{(g=1),t} S_{(g=2),t} \le W_{n,3,t} \end{cases} \tag{33}$$

The nonlinearity in Eq. (32), caused by the multiplication of binary variables, is resolved using auxiliary binary variables.

Eqs. (40) and (41) determine the two rows ($(n\text{-}1)^{th}$ row and n^{th} row) that the value of PUG_t is in their range.

$$\sum_{n\in\Omega_{PUGseg}} W_{(n-1),k,t} PUGs_n \le PUG_t \le \sum_{n\in\Omega_{PUGseg}} W_{n,k,t} PUGs_n \quad \forall t \in T, \forall k \in \Omega_{Comb} \tag{40}$$

Eq. (41) ensures that only one element of $W_{n,k,t}$ becomes 1 at each interval.

$$\sum_{n\in\Omega_{PUGseg}} \sum_{k\in\Omega_{Comb}} W_{n,k,t} = 1 \quad \forall t \in \Omega_T \tag{41}$$

Eq. (42) linearly calculates the value of PB_t^{dcmf} using interpolation.

$$PB_t^{dcmf} = \left(\left((PUG_t - PUGs_n)/(PUGs_n - PUGs_{(n-1)})\right) \times \left(dp_{n,k,t} - dp_{(n-1),k,t}\right)\right) + dp_{(n-1),k,t} \tag{42}$$

Overall, Eqs. (32–42), binary variable $W_{n,k,t}$ and interpolation helps us find a single value for PB_t^{dcmf} by selecting two consecutive rows and one column of the 2D table at each interval. This is done according to PUG_t and the realized combination of $S_{g,t}$.

Eq. (43) ensures the BESS SOC limits for PFC:

$$0.2 + EB_t^{df} \le SOC_t \le 1 - EB_t^{cf} \tag{43}$$

Where EB_t^{df}/EB_t^{cf} denote the share of SOC for PFC. Since PB_t^{dcmf} is insignificant compared to that used for EM, the values for EB_t^{df}/EB_t^{cf} are chosen based on the most severe scenarios, which is sufficient for all scenarios.

3.7. Stochastic optimization for dealing with uncertainties

Two-stage stochastic optimization is commonly used for optimization. Scenario generation deals with the uncertainties. Scenario reduction avoids the intractability of the problem. In this paper, $S_{g,t}$ is the only first-stage variable, and its values remain constant for all scenarios during the second stage. Eq. (44) models the objective of a two-stage stochastic optimization problem.

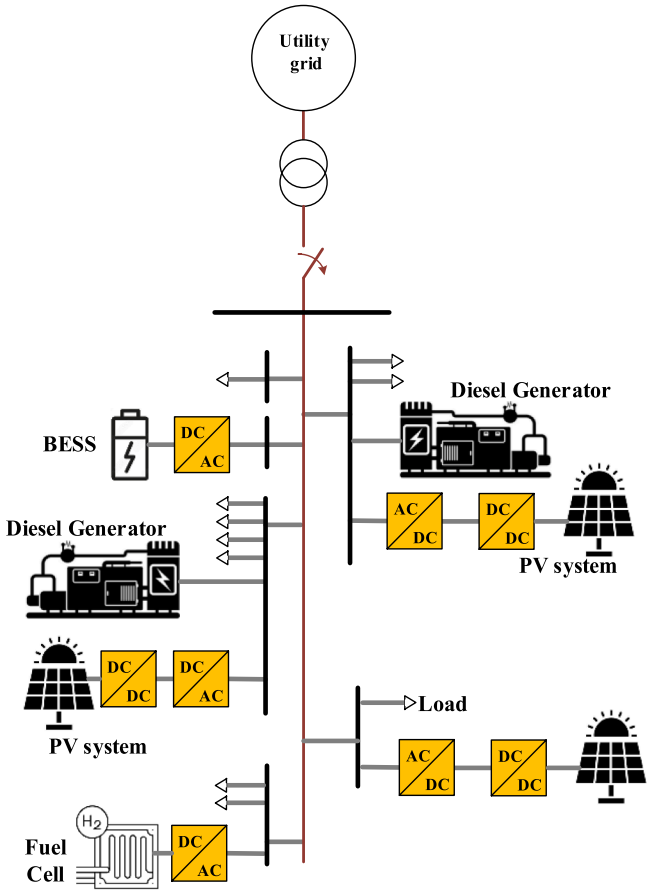

Fig. 14. AMG under study.

Table 1
Scenarios for Frequency simulation studies.

Scenario Group	Scenario	Grid power (kW)	PV MPP (kW)
1st	(a)	-20	0
	(b)	-20	6
	(c)	-20	18
2nd	(a)	20	18
	(b)	20	12
	(c)	20	9(both DEGs on), 6(one DEG on)

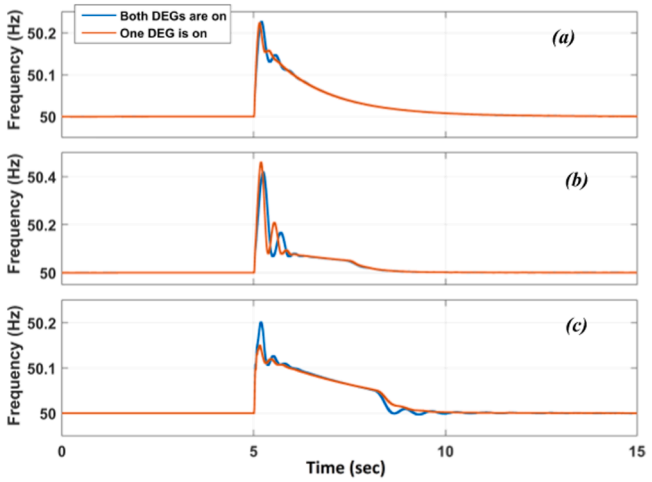

Fig. 15. AMG frequency response.

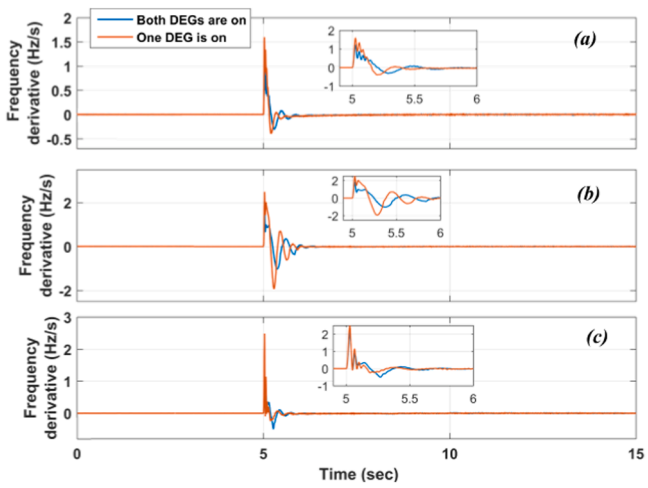

Fig. 16. AMG RoCoF.

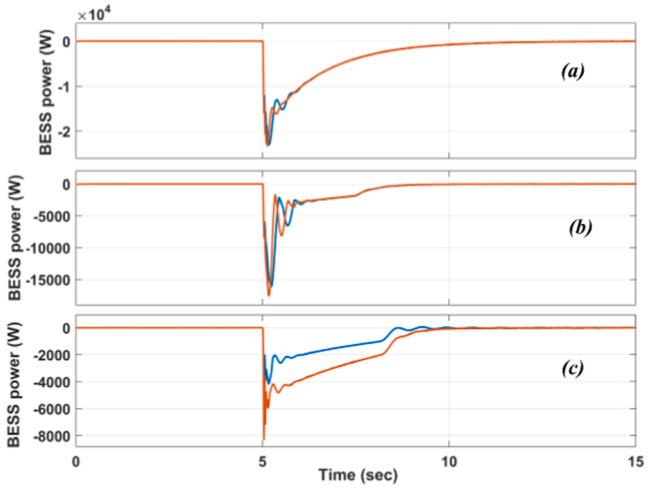

Fig. 17. BESS response.

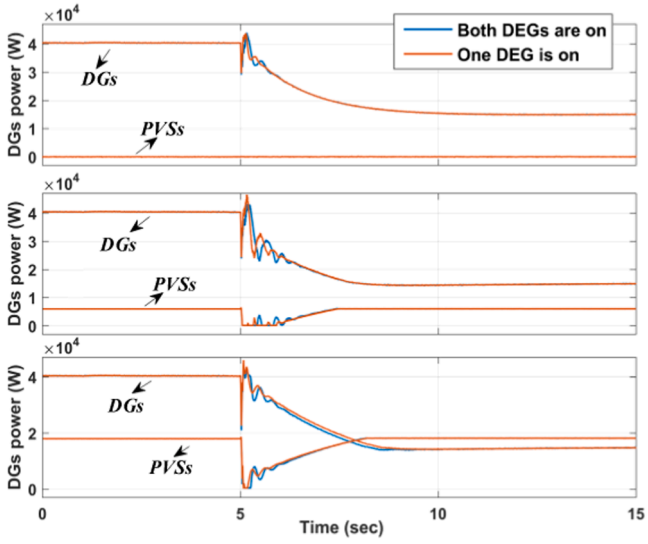

Fig. 18. DGs response.

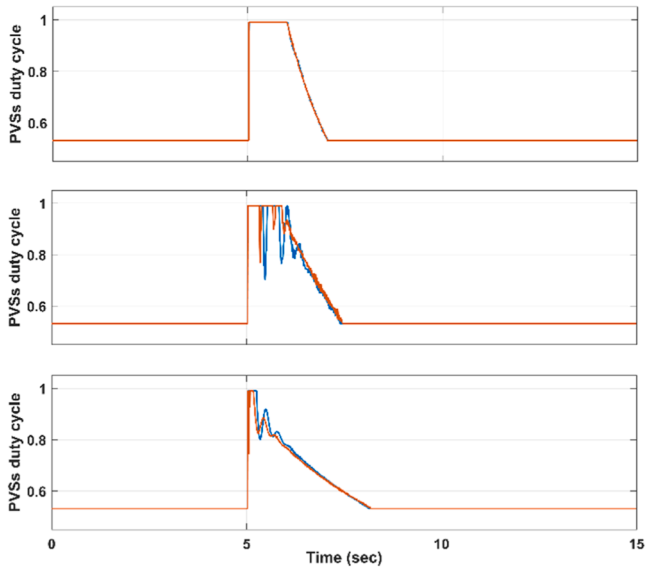

Fig. 19. Duty cycle of PVs converters.

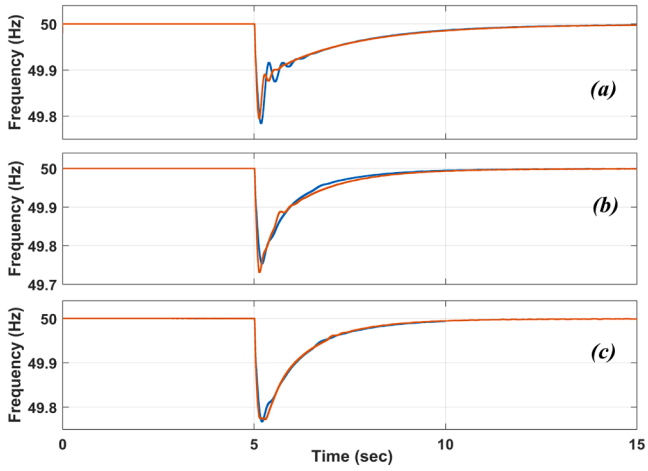

Fig. 20. AMG frequency response.

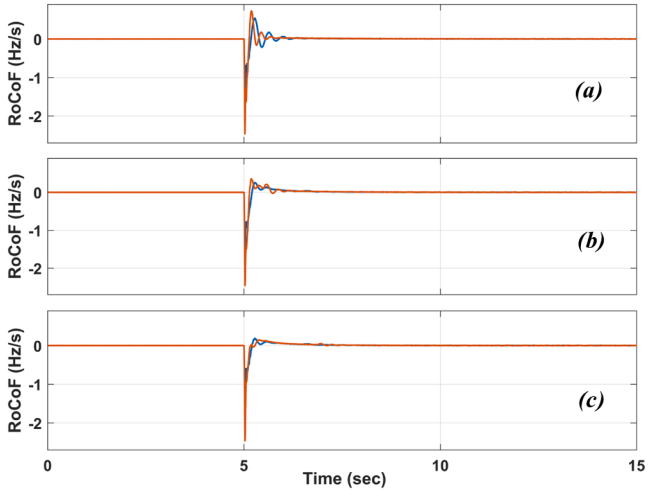

Fig. 21. AMG RoCoF.

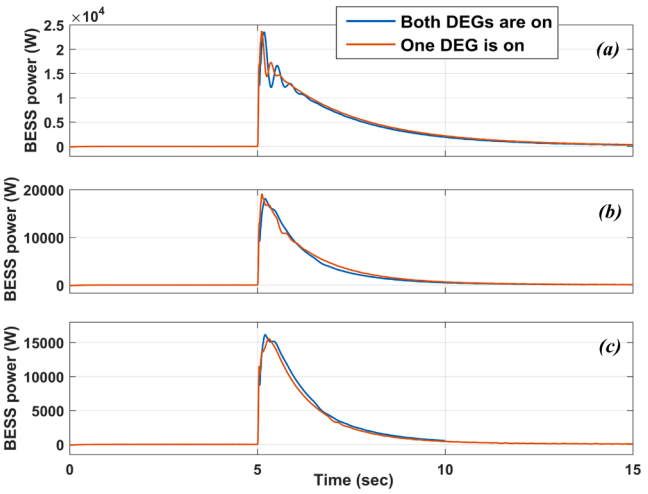

Fig. 22. BESS response.

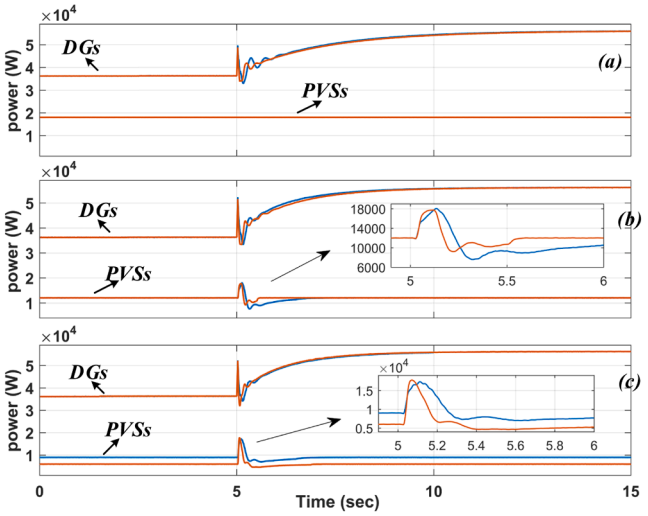

Fig. 23. DGs response.

Table 2
Results summary.

Scenario	No. of on DEGs	PB_t^{dcmf} (kW)	Scenario	No. of on DEGs	PB_t^{dcmf} (kW)
1(a)	2	-23.5	1(a)	1	-23.7
1(b)	2	-16.2	1(b)	1	-17.6
1(c)	2	-5.4	1(c)	1	-8.4
2(a)	2	23.5	2(a)	1	23.7
2(b)	2	17.6	2(b)	1	18.17
2(c)	2	16.4	2(c)	1	15.6

$$\min\left\{\sum_{t\in\Omega_T}\left(\sum_{t\in\Omega_{DG}}\left(SUG_{g,t}+SDG_{g,t}\right)\right)+\sum_{t\in\Omega_S}\rho_S TOCAM_S\right\} \tag{44}$$

where $TOCAM_S$ is the total operation cost of the AMG for each scenario that can be obtained from Eq. (2) minus DGs startup and shutdown costs, which are mentioned separately in Eq. (44) as they depend on $S_{g,t}$. Parameter ρ_S represents the probability of each scenario. It is of note that constraints (3–43) should be satisfied for each scenario.

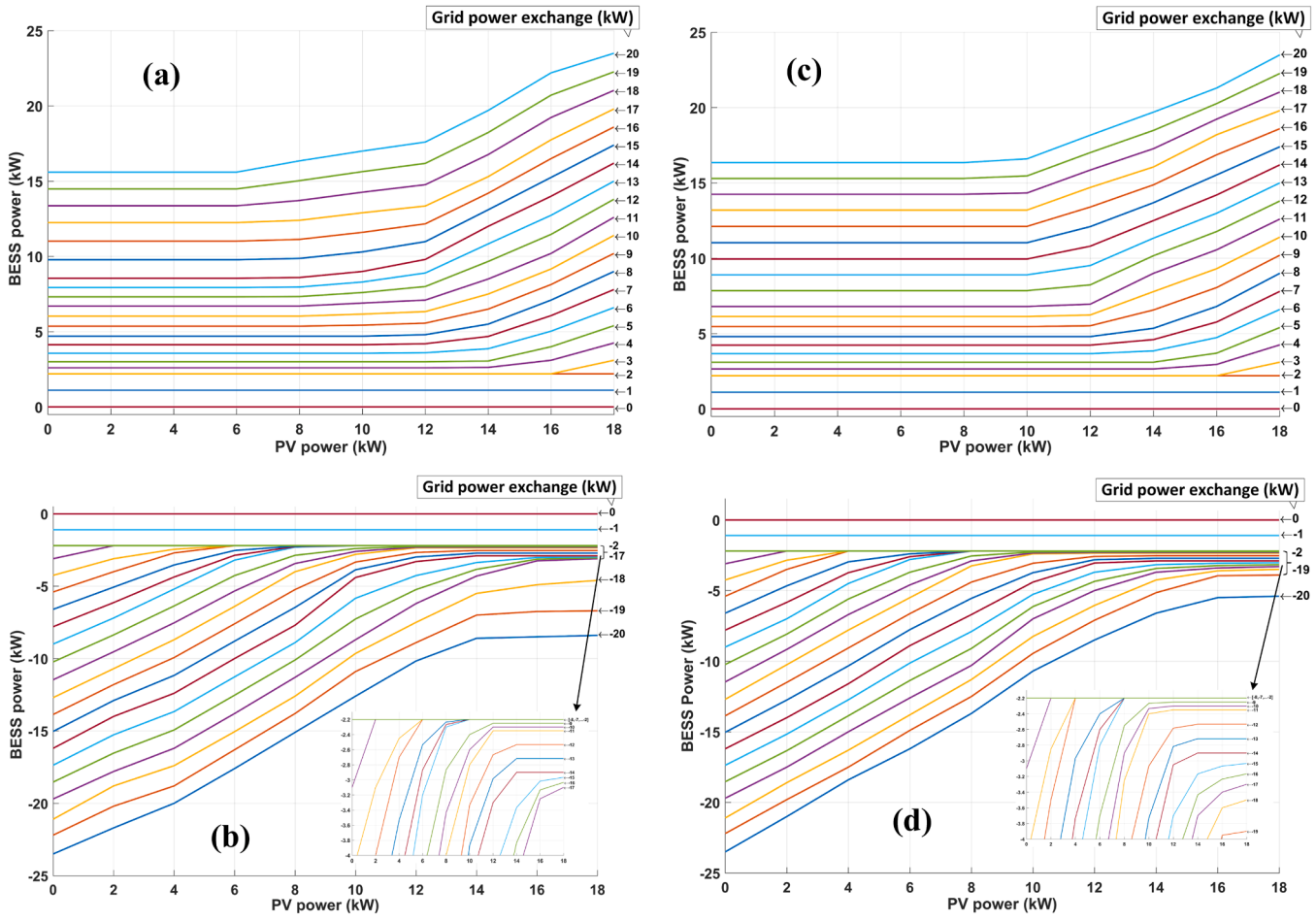

Fig. 24. The variation of required BESS reserve power (PB_t^{dcmf}) for PFC under different operation conditions (a) when both DEGs are on and power is imported from utility grid, (b) when both DEGs are on and power is exported to the utility grid, (c) when one DEG is on and power is imported from the utility grid, (d) when one DEG is on and power is exported to the utility grid.

Table 3
Operation and maintenance cost coefficients of DGs [46–48].

	a	b	c	d	e	f	M
$DEG_{1,2}$	0.000906	0.0264	1.13	0.018	0.000418	0.00403	0.01094
SOFC	0.000209	0.0232	0.33	0.0115	0.00000418	0.000109	0.00511
PVSs	-	-	-	-	-	-	0.00078

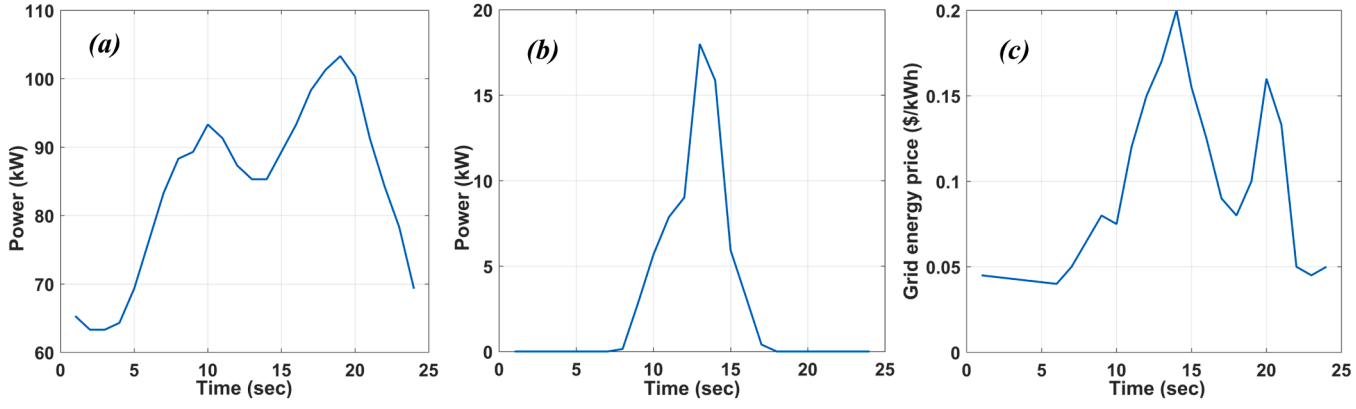

Fig. 25. Daily profiles, (a) Power demand, (b) PVSs power generation, (c) grid energy price.

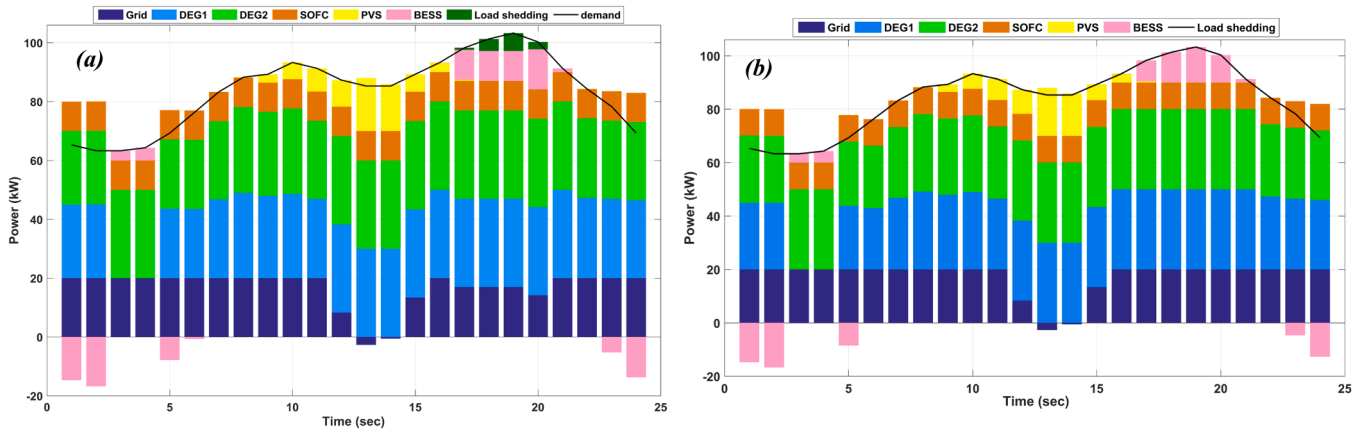

Fig. 26. Power variation of resources (a) without PVSs participation, (b) with PVSs participation in PFC.

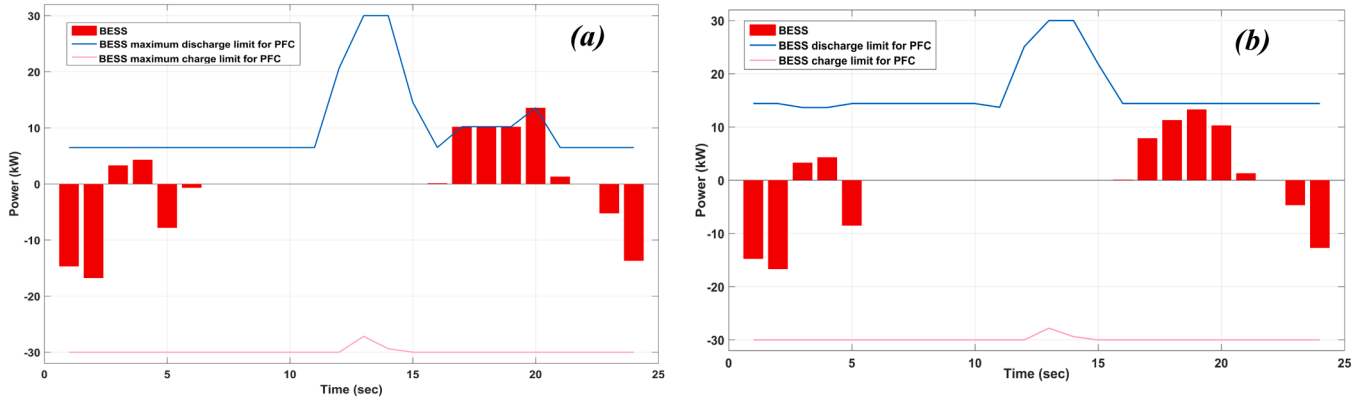

Fig. 27. BESS power and its varying discharge/charge limits (a) without PVSs participation, (b) with PVSs participation in the PFC.

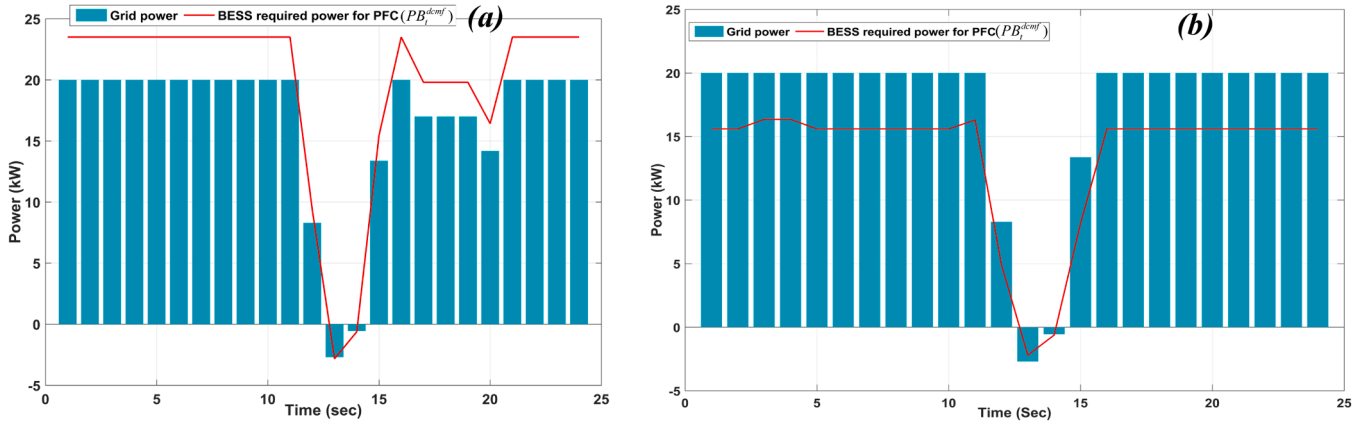

Fig. 28. Grid power exchange and the required BESS power for PFC (a) without PVSs participation, (b) with PVSs participation in the PFC.

4. Frequency simulation studies

This section focuses on frequency simulation of the CIGRE AMG test system, which is used in [23,41,42] and shown in Fig. 14. Matlab/Simulink software is used for the simulation studies. The results are used later for solving the problem of optimal AMG operation. The AMG under study consists of residential loads, two 31.1-kW diesel generators, a 10-kW solid-oxide fuel cell (SOFC), a 30 kW/60kWh Lithium-ion BESS. The DEG model, which is based on [43], is equipped with the 31.1 kW SG model that is available in Matlab/Simulink. SOFC model is taken from [44]. There are also three PVSs with power ratings of 8 kW, 5 kW, and 5 kW. The time constant of HPF in PVSs control system is 0.25 s. The FDBs are 49.95 Hz and 50.05 Hz. Maximum allowable power exchange with the utility grid is 20 kW. The non-renewable DGs can be dispatched to change their power generation for EM, and they are also locally controlled to perform PFC.

Table 1 lists some scenarios for simulation studies. The disturbance is unplanned islanding. In all results, blue color represents scenarios with both DEGs on while dark orange color shows scenarios where only one is on. In Scenarios marked with (a), PVSs do not participate in PFC. The control coefficients of PVSs and DGs are invariable, while those of BESS could vary in each scenario, aiming to decrease PB_t^{dcmf}. For this purpose, optimization (Genetic algorithm) is used. For scenarios with similar grid power exchange, one scenario is optimally tuned using optimization

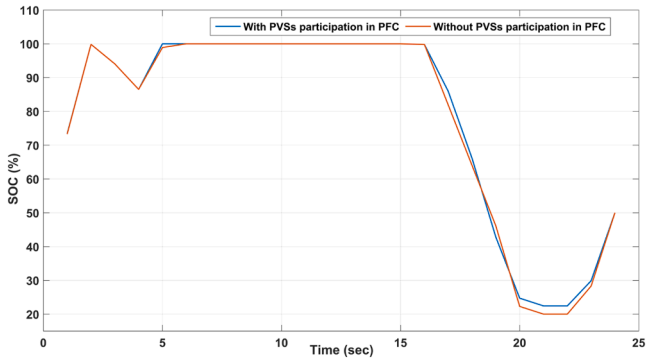

Fig. 29. SOC profile.

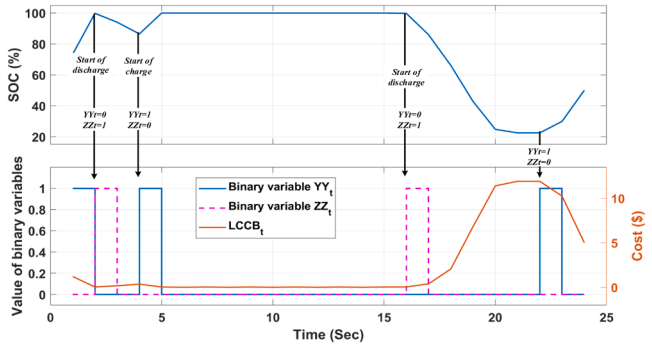

Fig. 30. Variation of binary variables YY_t and ZZ_t according to SOC profile.

while the trial and error approach is used for the rest.

4.1. 1st-group scenarios

The AMG is selling 20 kW to the utility grid. After unintentional islanding at the 5th second, the AMG experiences 20 kW of power surplus. Figs. 15–19 show the simulation results of scenarios (a), (b), and (c). To perform PFC, the BESS absorbed power, and the PVSs decreased their generation quickly. The dispatchable DGs gradually decreased their generation to perform SFC to restore the frequency.

The sum of PVSs in Fig. 18 shows that more PVSs power reduction leads to a greater decrease in BESS power. Notably, the PVSs deviate from the MPP for only two seconds, and the PFC of PVSs hardly affects their optimal operation. Moreover, Figs. 18 and 19 show that the duty cycle is controlled to provide maximum participation of PVSs in all scenarios regardless of their MPP. The results also show that as the frequency exceeds 50.05 Hz, the duty cycles and PVSs power return to the corresponding MPP value, which shows the FDB function.

4.2. 2nd-group of scenarios

While receiving 20 kW from the utility grid, the AMG is islanded, experiencing 20 kW of power shortage. The simulation results of scenarios (a), (b), and (c) are presented in Figs. 20–23. It can be seen in Figs. 20 and 21, that in all scenarios, the frequency and RoCoF are kept within their safe limits. Figs. 22 and 23 show that the less MPP leads to more PVSs power injection and hence a greater decrease in the BESS maximum power for PFC. Fig. 23 (c) shows that regardless of the MPP value, the PVSs provide maximum participation according to Fig. 6.

4.3. Analysis and summarization of frequency simulation studies

Table 2 summarizes the BESS performance in frequency simulation studies.

More simulation studies are done to obtain the value of PB_t^{dcmf} under different operational conditions. Grid power exchange varies from 20 kW to 20 kW, decreasing by 2 kW increments. Similarly, PVSs power varies from 0 kW to 18 kW, increasing by 2 kW increments. Both possible combinations of $S_{g,t}$ variation are considered too. The first combination is that one of the DEGs is on, and it does not differ which one, as both DEGs are similar. The other combination is that both SGs are on. It is worth noting that the connection of both DEGs or just one of them to the AMG affects the overall AMG inertia, the frequency variations and the required BESS reserve for PFC.

Simultaneously considering the variation of PVSs power, grid power exchange and $S_{g,t}$, there would be 420 ($=21 \times 10 \times 2$) scenarios. Also, 400 more scenarios were added with random values of these variables. Therefore, in total, 820 scenarios are simulated. As a result, Figs. 24–37 (a-d) are obtained, which represent the 3D table in Fig. 10. Data of Fig. 38 (a) and (b) can be used for when both DEGs are on while data of Fig. 24 (c) and (d) is for when only one of them is on. For any scenario, PB_t^{dcmf} can be obtained through interpolation of the data of these figures, as explained in Section 3.6. Notably, PVSs generation of 0 kW and 18 kW provide no participation in PFC in surplus scenarios and power shortage scenarios, respectively. These two scenarios can be compared with those in which PVSs participate in FC with different values of PVSs generation. This helps to compare the effectiveness of PVSs participation in FC.

Test scenarios were randomly generated to test the accuracy of the interpolation. Overall, the absolute amount of PB_t^{dcmf} was less than or

Table 4
Numerical summary of AMG operation costs.

PVSs participating in FC?	*OCDGS*(€)	*CUG*(€)	*CDBAT*(€)	*CLS*(€)	*TOCA* (€)
Yes	180.526	28.134	10.461	0	219.12
No	180.688	26.619	10.96	70.11	288.38

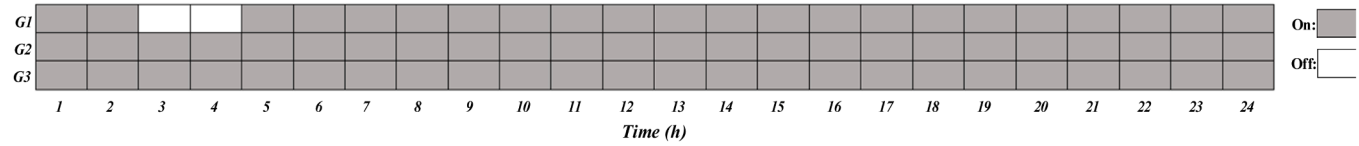

Fig. 31. Values of $S_{g,t}$ when PVSs participated in PFC.

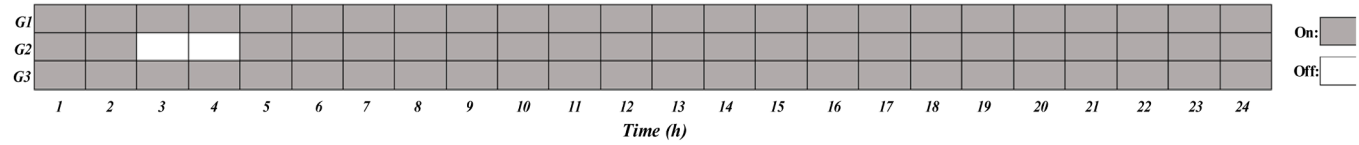

Fig. 32. Values of $S_{g,t}$ when PVSs did not participate in PFC.

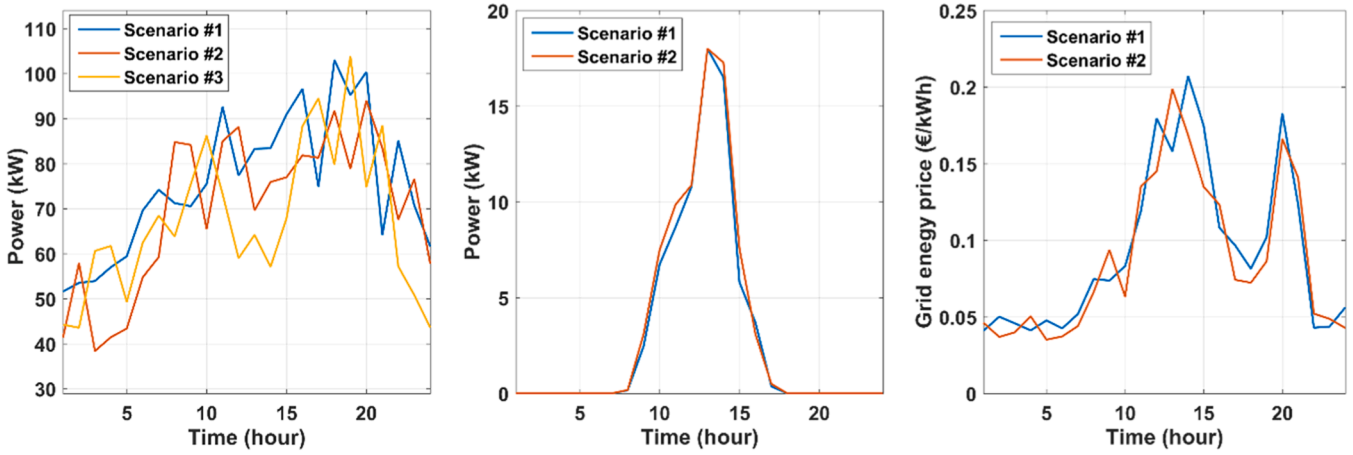

Fig. 33. Daily profiles, (a) Power demand, (b) PVSs power generation, (c) Grid energy price.

Table 5
Numerical summary of AMG operation costs.

Stochastic scenario No.	Demand scenario No.	PVSs power scenario No.	Energy price scenario No.	Probability
1	1	1	1	0.1298
2	1	1	2	0.13244
3	1	2	1	0.05999
4	1	2	2	0.06119
5	2	1	1	0.07698
6	2	1	2	0.07851
7	2	2	1	0.0797
8	2	2	2	0.08133
9	3	1	1	0.10121
10	3	1	2	0.10322
11	3	2	1	0.04727
12	3	2	2	0.04821

equal to the absolute value that was obtained from the interpolation, which always guarantees the frequency security.

Using the results of frequency simulation studies, the 3-DIM table in Fig. 10 is formed as shown in Fig. 24 (a-d), which is necessary for solving the problem of optimal AMG operation with frequency security constraint. In the next section, this problem is addressed and solved.

5. Optimal AMG operation considering frequency security constraint

In this section, the AMG optimal operation problem in this paper is solved as an MILP problem using GAMS software and CPLEX solver. The globally optimal solution can be obtained if the input data are globally optimal. A part of input data to this problem is the data of Fig. 24 which guarantees the AMG frequency security under different operation conditions. These input data may not be globally optimal as a metaheuristic optimization method is used to obtain them. The operation and maintenance cost coefficients of DGs are listed in Table 3. The load shedding cost is 5.22€/kWh. The startup cost is €0.13 for DEGs and €0.365 for the SOFC [45]. The price of selling energy to the grid is 0.009€ less than the buying price.

A deterministic approach is used to clearly show how the required power of BESS for PFC affects the optimal operation of the AMG in grid-connected mode. Also, stochastic optimization is used to model uncertainties.

5.1. Deterministic optimization

The daily profiles of power demand, PVSs power generation, and grid energy price are shown in Fig. 25, which are taken from references [49,

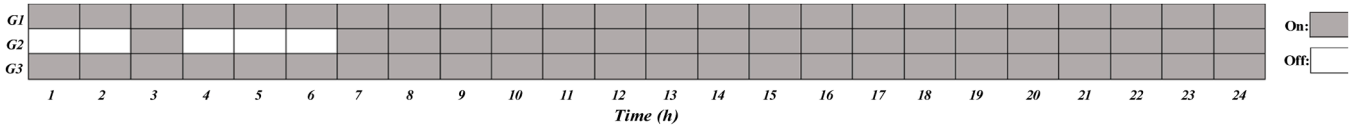

Fig. 34. On/Off states of DEGs without PVSs participation in PFC.

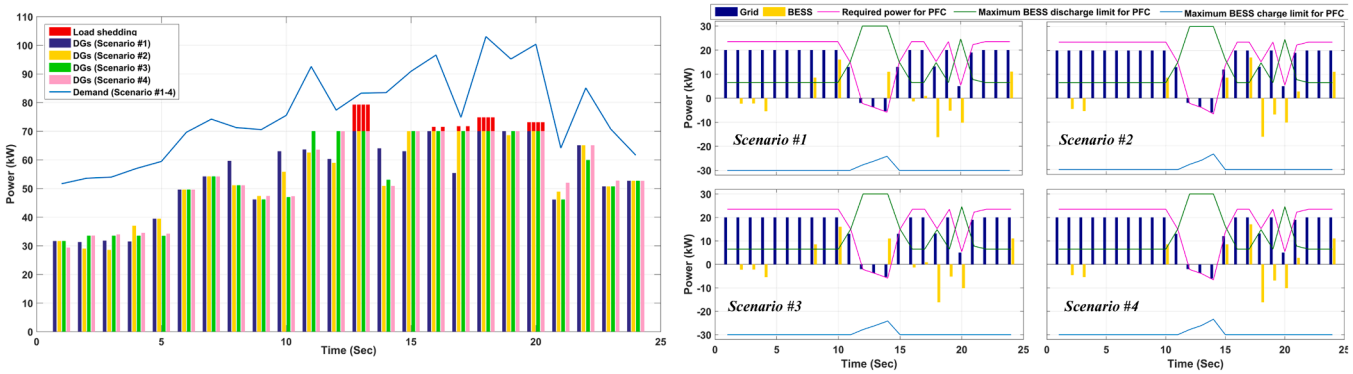

Fig. 35. Power variation of resources (scenarios 1–4).

50], respectively.

Fig. 26 (a-b) show the power generation of resources, which shows that the balance between generation and consumption has been maintained. Moreover, the amount of power generation is almost the same in both cases. During off-peak periods, the battery tends to charge to release energy during peak periods.

Unlike Fig. 26 (a), Fig. 26 (b) shows no load shedding due to the PVSs participation in PFC that reduces the required BESS reserve power for PFC. In this regard, Fig. 27 (a) shows that BESS has reached it maximum discharge power limit as opposed to that in Fig. 27 (b). In particular, the BESS participation has increased in EM relatively and has avoided load shedding from the 17th hour till the 20th hour due to the PVSs' participation in the PFC. This proves that the overall participation of the BESS in EM is less limited when PVSs participate in PFC. The blue and the pink curves in Fig. 27 (a) and (b) represent the values of the variable PB_t^{dcmf} in Eqs. (30) and (31). As BESS discharge power in Fig. 27 (a) reaches the limits during the 17th and 20th hour, the grid power exchange in Fig. 28 (a) becomes limited too. This is because the increase in

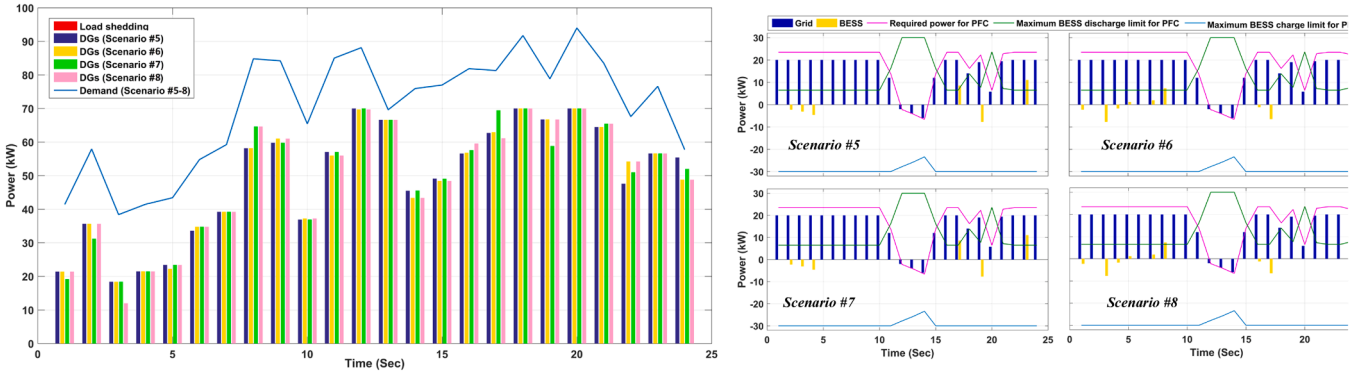

Fig. 36. Power variation of resources (scenarios 5–8).

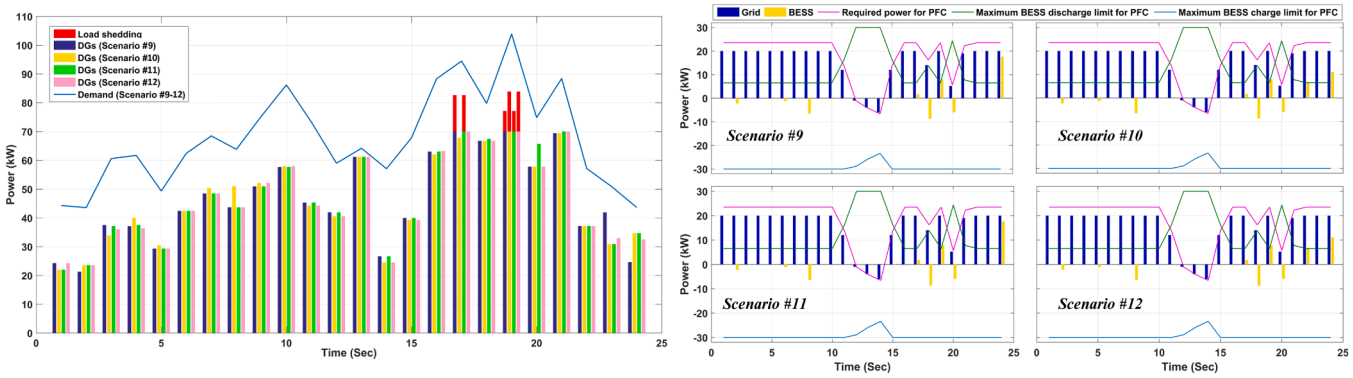

Fig. 37. Power variation of resources (scenarios 9–12).

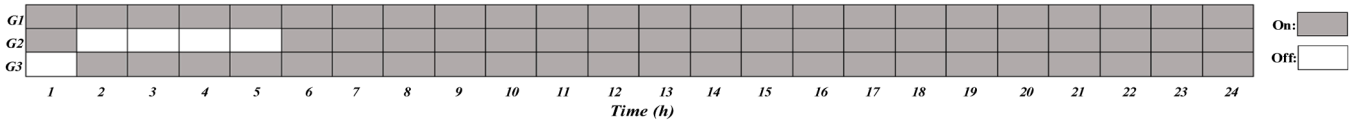

Fig. 38. On/Off states of DEGs with PVSs participation in PFC.

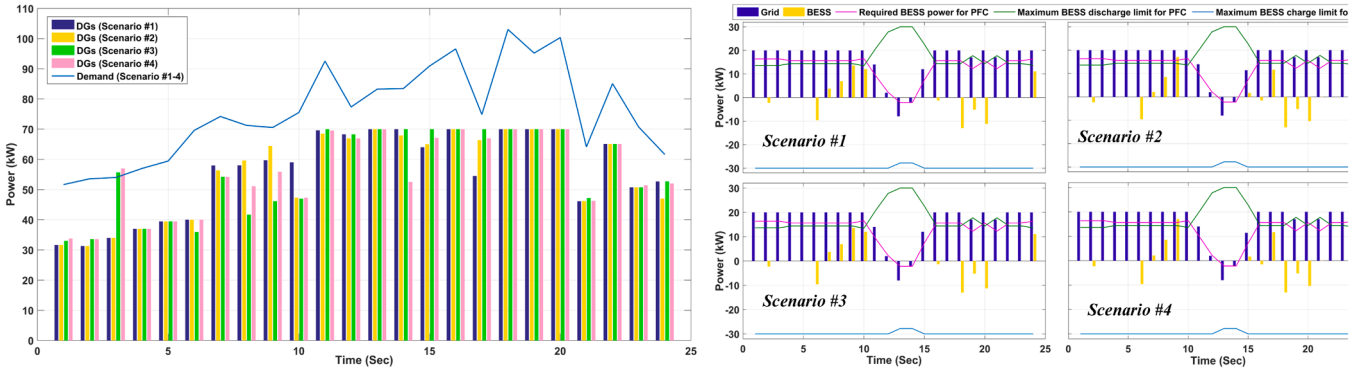

Fig. 39. Power variation of resources (scenarios 9–12).

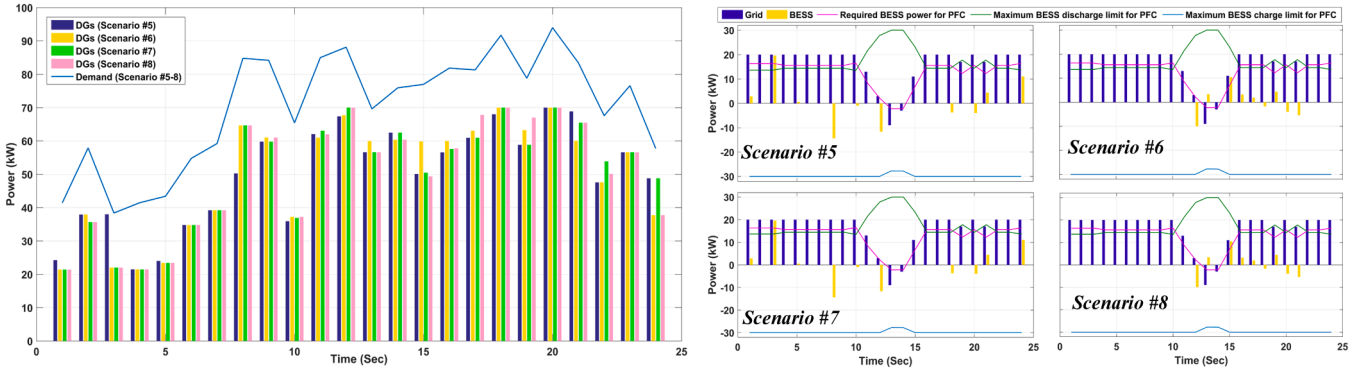

Fig. 40. Power variation of resources (scenarios 9–12).

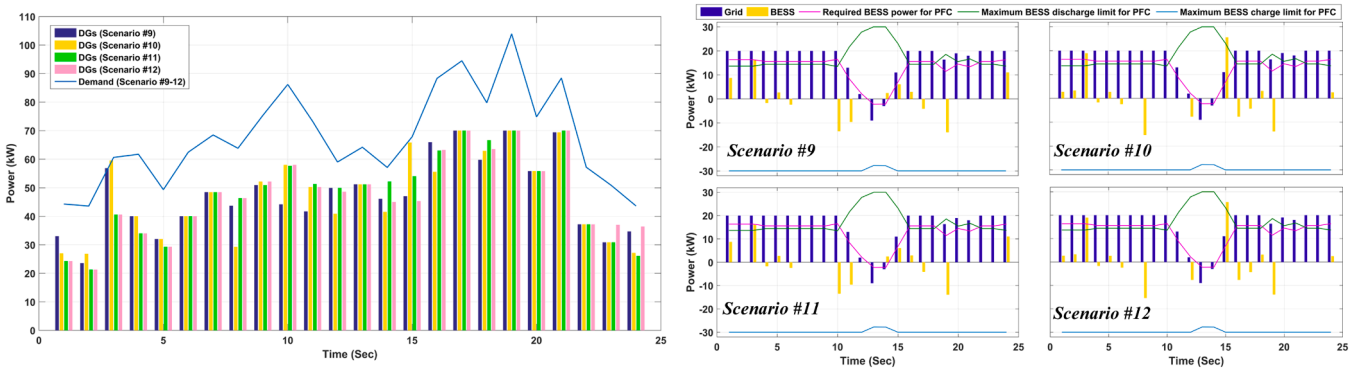

Fig. 41. Power variation of resources (scenarios 9–12).

the grid power exchange leads to an increase in PB_t^{dcmf} which is not possible. However, this is not the case for either the BESS in Fig. 27 (b) or the grid power in Fig. 28 (b).

The battery SOC shown in Fig. 29 varies almost similarly for both cases. For the case when PVSs participate in PFC, Fig. 30 shows how the SOC profile and relative binary variables are applied to calculate the BESS degradation cost.

Figs. 31 and 32 demonstrates the on/off states of DEGs during each interval.

The detailed costs of AMG operation are listed in Table 4. It can be seen that the PVs participation in PFC decrease the AMG operation cost by €69.258 (about 24 % reduction) compared to when the PVSs did not participate in PFC. It is worth noting that the mentioned amount of cost reduction is majorly due to preventing load shedding. In this regard, the load shedding cost of €70.11 approximately equals the overall cost difference of the two studied cases.

5.2. Stochastic optimization

To model uncertainties, 1000 scenarios are generated for each of the demand, the PVSs power, and the grid energy price. The Normal distribution is used for modeling the uncertainty of the load demand and the energy price while the beta distribution is used for PVSs. The stochastic variations from their predicted values are 20 %, 15 % and 10 %, respectively [50,51]. Then, the backward reduction technique is used to reduce scenarios to make the problem tractable [50]. In this regard, Fig. 33 shows reduced scenarios of the demand, PVSs power and grid energy price, respectively. In these figures, the original scenarios are similar to the data/curves which are available in [49,50,52], respectively. Each stochastic scenario and its corresponding probability is listed in Table is given in Table 5. According to equation (47), the AMG cost of all scenarios is simultaneously minimized.

For scenarios in which PVSs have not participated in PFC, Fig. 34 shows the on/off states of DGs while Figs. 35–37 show the power variation of resources and the variation of PB_t^{dcmf}. The balance between demand and supply is optimally maintained in all scenarios. When the energy price is relatively low, the BESS charges and energy is received from the grid, and vice versa. For all scenarios except 5–8, the BESS power reached its maximum power discharge limit in certain periods, like 17th-20th hours. During these hours, the DGs capacity is not sufficient either, which makes load shedding unavoidable.

For scenarios in which PVSs have participated in PFC, Fig. 38 shows the on/off states of DGs and Figs. 39–41 depict the power variation of DGs, BESS, and the variation of PB_t^{dcmf}. It is evident that no load shedding is required because the BESS discharge limits are not reached. This shows that PVSs participation in PFC allows more effective participation of the BESS and the utility grid in EM. While the BESS and the utility grid powers have remained unchanged during some periods in the scenarios, they have also changed in some other periods. For instance, the BESS power has increased in scenario 1 and 3 during the 9th hour.

The value of the objective function in equation (47) is €185.098 when PVSs participates in PFC, showing €59.102 (about 24.2 %) decrease compared to €244.2 when PVSs do not participate in PFC.

6. Conclusion and future work

A linear model was proposed for solving the problem of optimal operation of a grid-connected AMG while maintaining frequency security. As a significant part of the BESS reserve power for PFC is used quickly, it is proposed that the PVSs provide HFCs of the required power for PFC to decrease the maximum required BESS power for this task. This is advantageous since PVSs do not always operate at their power rating point and therefore, they can shortly increase their power generation by releasing DLC energy in power shortage conditions. Also, PVSs can

decrease their output power in power surplus conditions. Simulation results indicated more effective participation of the BESS in EM through this approach.

HPFs and FDBs were used in the PVSs controllers to use them shortly and avoid them during minor frequency disturbances. This means that PVSs hardly deviate from MPPs. Importantly, PVSs are used for PFC without adding new hardware.

The obtained optimization results of the AMG optimal operation problem showed that without PVSs assist in PFC, BESS, utility grid and other AMG resources were not always sufficient to supply the whole demand. Therefore, load shedding became necessary in some periods to first ensure both optimal operation and frequency security of the AMG. This is because, as the utility grid power exchange increased, more power reserve was required for PFC. When PVSs did not participate in PFC, BESS had to provide all necessary reserve power for PFC, which relatively reduced the participation of the BESS and the utility grid in the AMG EM. On the other hand, the BESS or the utility grid participated in the AMG EM when PVSs assisted in PFC. In particular, the deterministic optimization showed the increase in the participation of the BESS in EM. This avoided load shedding and hence, decreased the AMG operation. Results from the deterministic optimization showed that the total cost of AMG operation could be reduced by 24 %, while stochastic optimization achieved a reduction of 24.2 %. Therefore, the brief participation of PVSs in the AMG PFC can have considerable economic benefit.

The current work ensures the AMG frequency security just few minutes after islanding. However, the AMG may still face various types of frequency events including demand/generation variation/outage, cyberattacks and etc. To ensure safe and continuous supply of power to consumers in islanded mode, further research work is proposed to model the optimal islanded operation with frequency security constraints after safe islanding.

Moreover, the number of synchronous generators, the BESS size and the PVSs penetration rate affect both PFC and EM. Future works can do sensitivity analysis on the penetration rate of PVSs, BESS size and the number of synchronous generators in the AMG to understand how these affect the AMG optimal operation and its cost.

Furthermore, DLCs have limited energy. Using a supercapacitor, instead, much more power can be injected to the AMG in power shortage conditions and the maximum required BESS power for PFC can be further decreased. However, the cost of supercapacitor should also be taken into account.

CRediT authorship contribution statement

Marjan Popov: Writing – review & editing, Supervision. **Mehrdad Bagheri-Sanjareh:** Writing – original draft, Visualization, Validation, Software, Resources, Project administration, Methodology, Investigation, Formal analysis, Data curation, Conceptualization.

Declaration of Competing Interest

The authors declare that they have no known competing financial interests or personal relationships that could have appeared to influence the work reported in this paper.

Data availability

All data and parameters are available in the paper

References

[1] A. Salari, S.E. Ahmadi, M. Marzband, M. Zeinali, Fuzzy Q-learning-based approach for real-time energy management of home microgrids using cooperative multi-agent system, Sustain. Cities Soc. 95 (2023) 104528.
[2] E.E. Pompodakis, G.I. Orfanoudakis, G. Katsigiannis, A. Tsikalakis, E. Karapidakis, A novel power flow approach for calculating the steady-state of secondary control in islanded microgrids under cyberattacks, Sustainable Energy, Grids Netw. 42 (2025) 101646.
[3] S. Lim, T. Kim, K.Y. Lee, D. Choi, J.-W. Park, Impact of high penetration of renewables on power system frequency response: a review and verification, Renew. Sustain. Energy Rev. 217 (2025) 115728.
[4] A. Hadavi, M.T. Hagh, S.G. Zadeh, Critical inertia thresholds for frequency stability in renewable Energy-Integrated power systems, Int. J. Electr. Power Energy Syst. 169 (2025) 110733.
[5] A. Mohamed, E.M. Wazeer, S.M. El Masry, A.A. Ghany, M.A. Mosa, A novel scheme of load frequency control for a multi-microgrids power system utilizing electric vehicles and supercapacitors, J. Energy Storage 89 (2024) 111799.
[6] A. Khalil, Z. Rajab, A. Alfergani, O. Mohamed, The impact of the time delay on the load frequency control system in microgrid with plug-in-electric vehicles, Sustain. Cities Soc. 35 (2017) 365–377.
[7] M.A. Hossain, R.K. Chakrabortty, M.J. Ryan, H.R. Pota, Energy management of community energy storage in grid-connected microgrid under uncertain real-time prices, Sustain. Cities Soc. 66 (2021) 102658.
[8] M. Bagheri Sanjareh, M.H. Nazari, S.H. Hosseinian, A novel strategy for frequency control of islanded greenhouse with cooperative usage of BESS and LED lighting loads, Electr. Eng. 103 (2021) 265–277.
[9] U. Tamrakar, T.M. Hansen, R. Tonkoski, D.A. Copp, Model predictive frequency control of low inertia microgrids, in: 2019 IEEE 28th International Symposium on Industrial Electronics (ISIE), IEEE, 2019, pp. 2111–2116.
[10] M.H. Nazari, M. Bagheri-Sanjareh, S.H. Hosseinian, A new method for energy management of residential microgrid for sizing electrical and thermal storage systems, Sustain. Cities Soc. 76 (2022) 103482.
[11] M. Liu, W. Li, C. Wang, M.P. Polis, L.Y. Wang, J. Li, Reliability evaluation of large scale battery energy storage systems, IEEE Trans. Smart Grid 8 (2016) 2733–2743.
[12] P.C. Sahu, S. Mishra, R.C. Prusty, S. Panda, Improved-salp swarm optimized type-II fuzzy controller in load frequency control of multi area islanded AC microgrid, Sustain. Energy Grids Netw. 16 (2018) 380–392.
[13] A. Jani, H. Karimi, S. Jadid, Hybrid energy management for islanded networked microgrids considering battery energy storage and wasted energy, J. Energy Storage 40 (2021) 102700.
[14] M. Shimillas, B.V. Venkatasubramanian, N. Hatziargyriou, M. Panteli, Anticipatory distribution network reconfiguration: a decision-support framework for networked microgrids formation and energy management, Sustain. Energy Grids Netw. (2025) 101804.
[15] M.M. Mohamed, H.M. El Zoghby, S.M. Sharaf, M.A. Mosa, Optimal virtual synchronous generator control of battery/supercapacitor hybrid energy storage system for frequency response enhancement of photovoltaic/diesel microgrid, J. Energy Storage 51 (2022) 104317.
[16] O.N. Onsomu, E. Terciyanlı, B. Yeşilata, Comprehensive review of energy management strategies: considering battery energy storage system and renewable energy sources, Eng. Rep. 6 (2024) e12995.
[17] Y. Wen, C. Chung, X. Liu, L. Che, Microgrid dispatch with frequency-aware islanding constraints, IEEE Trans. Power Syst. 34 (2019) 2465–2468.
[18] M. Javadi, Y. Gong, C. Chung, Frequency stability constrained microgrid scheduling considering seamless islanding, IEEE Trans. Power Syst. 37 (2021) 306–316.
[19] A. Sangwongwanich, Y. Yang, F. Blaabjerg, A sensorless power reserve control strategy for two-stage grid-connected PV systems, IEEE Trans. Power Electron. 32 (2017) 8559–8569.
[20] Z. Li, Z. Cheng, J. Si, S. Zhang, L. Dong, S. Li, Y. Gao, Adaptive power point tracking control of PV system for primary frequency regulation of AC microgrid with high PV integration, IEEE Trans. Power Syst. 36 (2021) 3129–3141.
[21] H. Xin, Y. Liu, Z. Wang, D. Gan, T. Yang, A new frequency regulation strategy for photovoltaic systems without energy storage, IEEE Trans. Sustain. Energy 4 (2013) 985–993.
[22] D. Wu, F. Tang, T. Dragicevic, J.C. Vasquez, J.M. Guerrero, Autonomous active power control for islanded ac microgrids with photovoltaic generation and energy storage system, IEEE Trans. Energy Convers. 29 (2014) 882–892.
[23] M. Bagheri-Sanjareh, M.H. Nazari, G.B. Gharehpetian, A novel and optimal battery sizing procedure based on MG frequency security criterion using coordinated application of BESS, LED lighting loads, and photovoltaic systems, IEEE Access 8 (2020) 95345–95359.
[24] X. Lyu, Z. Xu, J. Zhao, A coordinated frequency control strategy for photovoltaic system in microgrid, J. Int. Counc. Electr. Eng. 8 (2018) 37–43.
[25] M.A. Mosa, M.Y. Yousef, S.M. El Masry, A.A. Ghany, A. Ali, Frequency support of AC microgrid with high penetration of photovoltaic using super-capacitor, Sustain. Energy Technol. Assess. 53 (2022) 102364.
[26] C. Wang, F. Yang, Z. Zhang, K. Qian, H. Lin, Y. Cao, Photovoltaic-storage coordinated support control technology based on primary frequency regulation requirements, Energy Rep. 12 (2024) 6126–6136.
[27] D. Xu, Z. Wu, L. Zhu, L. Guan, A novel frequency constrained unit commitment considering VSC-HVDC's frequency support in asynchronous interconnected system under renewable energy Source's uncertainty, Electr. Power Syst. Res. 238 (2025) 111098.
[28] G. Sun, Q. Wang, S. Chen, Z. Wei, H. Zang, Look-ahead dispatch of power systems based on linear alternating current optimal power flow framework with nonlinear frequency constraints using physics-informed neural networks, J. Mod. Power Syst. Clean. Energy (2024).
[29] J. Liu, C. Wang, J. Zhao, T. Bi, Rocof constrained unit commitment considering spatial difference in frequency dynamics, IEEE Trans. Power Syst. 39 (2023) 1111–1125.

[30] J.-J. Wu, G.W. Chang, C. Sinatra, P.-Y. Tsai, Unit commitment with frequency stability enhancement for an isolated power system, IEEE Access 12 (2024) 91396–91409.
[31] W.S. Alvarez, J.C. López, F.W. Liederer, D. Dotta, M.J. Rider, Dynamic security constrained AC optimal power flow for microgrids, Electr. Power Syst. Res. 236 (2024) 110927.
[32] Y. Yang, C. Su, Q. Tan, S. Han, R. Zhang, Y. Cui, Short-term optimal scheduling of a cascade hydropower-wind-photovoltaic-concentrated solar power hybrid power system considering dynamic frequency security constraints and flexible load response, Energy Convers. Manag. 347 (2026) 120560.
[33] M. Bagheri-Sanjareh, M.H. Nazari, M. Amini, S.H. Hosseinian, S.M.S. Ghiasi, Enabling PV systems to participate in frequency regulation of islanded microgrids considering the effect of shading on solar irradiance and PV temperature, in: 2022 12th Smart Grid Conference (SGC), IEEE, 2022, pp. 1–6.
[34] M.B. Sanjareh, M.H. Nazari, G.B. Gharehpetian, S.M.S. Ghiasi, A novel strategy for optimal battery sizing based on MG frequency security criterion, in: 2019 international power system conference (PSC), IEEE, 2019, pp. 716–722.
[35] F. Moazeni, J. Khazaei, Optimal operation of water-energy microgrids; a mixed integer linear programming formulation, J. Clean. Prod. 275 (2020) 122776.
[36] M. Amini, M.H. Nazari, S.H. Hosseinian, Optimal energy management of battery with high wind energy penetration: a comprehensive linear battery degradation cost model, Sustain. Cities Soc. 93 (2023) 104492.
[37] I.N. Moghaddam, B. Chowdhury, M. Doostan, Optimal sizing and operation of battery energy storage systems connected to wind farms participating in electricity markets, IEEE Trans. Sustain. Energy 10 (2018) 1184–1193.
[38] M. Amini, A. Khorsandi, B. Vahidi, S.H. Hosseinian, A. Malakmahmoudi, Optimal sizing of battery energy storage in a microgrid considering capacity degradation and replacement year, Electr. Power Syst. Res. 195 (2021) 107170.
[39] J.-O. Lee, Y.-S. Kim, Novel battery degradation cost formulation for optimal scheduling of battery energy storage systems, Int. J. Electr. Power Energy Syst. 137 (2022) 107795.
[40] I. Serban, A control strategy for microgrids: seamless transfer based on a leading inverter with supercapacitor energy storage system, Appl. Energy 221 (2018) 490–507.
[41] N.W. Lidula, A.D. Rajapakse, Microgrids research: a review of experimental microgrids and test systems, Renew. Sustain. Energy Rev. 15 (2011) 186–202.
[42] M.B. Sanjareh, M.H. Nazari, G.B. Gharehpetian, R. Ahmadiahangar, A. Rosin, Optimal scheduling of HVACs in islanded residential microgrids to reduce BESS size considering effect of discharge duration on voltage and capacity of battery cells, Sustain. Energy Grids Netw. 25 (2021) 100424.
[43] V. Friedel, Modeling and simulation of a hybrid wind-diesel microgrid, in, 2009.
[44] Y. Zhu, K. Tomsovic, Development of models for analyzing the load-following performance of microturbines and fuel cells, Electr. Power Syst. Res. 62 (2002) 1–11.
[45] X. Wu, X. Wang, C. Qu, A hierarchical framework for generation scheduling of microgrids, IEEE Trans. Power Deliv. 29 (2014) 2448–2457.
[46] T. Adefarati, R. Bansal, M. Bettayeb, R. Naidoo, Optimal energy management of a PV-WTG-BSS-DG microgrid system, Energy 217 (2021) 119358.
[47] H. Moradi, M. Esfahanian, A. Abtahi, A. Zilouchian, Optimization and energy management of a standalone hybrid microgrid in the presence of battery storage system, Energy 147 (2018) 226–238.
[48] V. Murty, A. Kumar, Multi-objective energy management in microgrids with hybrid energy sources and battery energy storage systems, Prot. Control Mod. Power Syst. 5 (2020) 2.
[49] S. Kakran, S. Chanana, Operation management of a renewable microgrid supplying to a residential community under the effect of incentive-based demand response program, Int. J. Energy Environ. Eng. 10 (2019) 121–135.
[50] Z. Li, Y. Xu, Temporally-coordinated optimal operation of a multi-energy microgrid under diverse uncertainties, Appl. Energy 240 (2019) 719–729.
[51] B. Zhao, H. Qiu, R. Qin, X. Zhang, W. Gu, C. Wang, Robust optimal dispatch of AC/DC hybrid microgrids considering generation and load uncertainties and energy storage loss, IEEE Trans. Power Syst. 33 (2018) 5945–5957.
[52] M. Jalili, M. Sedighizadeh, A.S. Fini, Stochastic optimal operation of a microgrid based on energy hub including a solar-powered compressed air energy storage system and an ice storage conditioner, J. Energy Storage 33 (2021) 102089.